

Journal of Energy

ISSN 1849-0751 (On-line)
ISSN 0013-7448 (Print)
UDK 621.31

<https://doi.org/10.37798/EN2020692>

VOLUME 69 Number 2 | 2020

- 03** Martin Dadić, Tomislav Župan
Teaching Magneto-Thermal Coupling Using Thomson's Levitating Ring Experiment
- 11** Goran Levačić, Alain Xémard, Miroslav Mesić
Determination of Cumulative Distribution Function of the Crest Value of the Lightning Current Flowing Through Line Surge Arresters
- 19** Denisa Galzina, Eraldo Banovac, Tomislav Tomiša
Railway System Impact on Voltage Quality at the Level of the Croatian Transmission Network
- 24** Mićo Klepo, Vladimir Mikuličić, Zdenko Šimić
Peak Plant Models in the Electric Power System Model of Reliability and Availability

Journal of Energy

Scientific Professional Journal Of Energy, Electricity, Power Systems

Online ISSN 1849-0751, Print ISSN 0013-7448, VOL 68

<https://doi.org/10.37798/EN2020692>

Published by

HEP d.d., Ulica grada Vukovara 37, HR-10000 Zagreb

HRO CIGRÉ, Berislavićeva 6, HR-10000 Zagreb

Publishing Board

Robert Krklec, (president) HEP, Croatia,

Božidar Filipović-Grčić, (vicepresident), HRO CIGRÉ, Croatia

Editor-in-Chief

Goran Slipac, HEP, Croatia

Associate Editors

Helena Božić HEP, Croatia

Stjepan Car Green Energy Cooperation, Croatia

Tomislav Gelo University of Zagreb, Croatia

Davor Grgić University of Zagreb, Croatia

Marko Jurčević University of Zagreb, Croatia

Mičo Klepo Croatian Energy Regulatory Agency, Croatia

Stevo Kolundžić Croatia

Vitomir Komen HEP, Croatia

Marija Šiško Kuliš HEP, Croatia

Dražen Lončar University of Zagreb, Croatia

Goran Majstrovic Energy Institute Hrvoje Požar, Croatia

Tomislav Plavšić Croatian Transmission system Operator, Croatia

Dubravko Sabolić Croatian Transmission system Operator, Croatia

Mladen Zeljko Energy Institute Hrvoje Požar, Croatia

International Editorial Council

Murat Akpınar JAMK University of Applied Sciences, Finland

Anastasios Bakirtzis University of Thessaloniki, Greece

Eraldo Banovac J. J. Strossmayer University of Osijek, Croatia

Franjo Barbir University of Split, Croatia

Tomislav Barić J. J. Strossmayer University of Osijek, Croatia

Frank Bezzina University of Malta

Srećko Bojić Power System Institute, Zagreb, Croatia

Tomislav Capuder University of Zagreb, Croatia

Martin Dadić University of Zagreb, Croatia

Ante Elez Končar-Generators and Motors, Croatia

Dubravko Franković University of Rijeka, Croatia

Hrvoje Glavaš J. J. Strossmayer University of Osijek, Croatia

Mevludin Glavić University of Liege, Belgium

Božidar Filipović Grčić University of Zagreb, Croatia

Dalibor Filipović Grčić Končar-Electrical Engineering Institute, Croatia

Josep M. Guerrero Aalborg Universitet, Aalborg East, Denmark

Juraj Havelka University of Zagreb, Croatia

Dirk Van Hertem KU Leuven, Faculty of Engineering, Belgium

Žarko Janić Siemens-Končar-Power Transformers, Croatia

Igor Kuzle University of Zagreb, Croatia

Mislav Majstrovic University of Split, Croatia

Zlatko Maljković University of Zagreb, Croatia

Predrag Marić J. J. Strossmayer University of Osijek, Croatia

Viktor Milardić University of Zagreb, Croatia

Srete Nikolovski J. J. Strossmayer University of Osijek, Croatia

Damir Novosel Quanta Technology, Raleigh, USA

Hrvoje Pandžić University of Zagreb, Croatia

Milutin Pavlica Power System Institute, Zagreb, Croatia

Robert Sitar Hyundai Electric Switzerland Ltd. Zürich, Switzerland

Damir Sumina University of Zagreb, Croatia

Elis Sutlović University of Split, Croatia

Zdenko Šimić Joint Research Centre, Petten, The Netherlands

Damir Šljivac J. J. Strossmayer University of Osijek Croatia

Darko Tipurić University of Zagreb, Croatia

Bojan Trkulja University of Zagreb, Croatia

Nela Vlahinić Lenz University of Split, Croatia

Mario Vražić University of Zagreb, Croatia

EDITORIAL

This regular second issue in 2020 marks the 69th year of publishing the Journal of Energy. We are especially happy due to the fact that our Journal was included into INSPEC (Information Services for the Physics and Engineering Communities) citation database of journals. INSPEC is a bibliographical database published by the Institution of Engineering and Technology from London, and it indexes and contains works from the fields of physics, electrical engineering, computer science, information technology, technical sciences. That is a great motivation for the future work of the editorial board, to achieve better quality of works covering different topics of energy system.

The first paper is entitled as "Teaching Magneto-Thermal Coupling Using Thomson's Levitating Ring Experiment". The levitating ring experiment is presented as a method for teaching magneto-thermal interactions. The complete electromagnetic model of a problem is given, together with the insight in thermal analysis. The factors for determining the vertical displacements are explained, and an elegant method for indirect measurement of induced current in the ring is introduced. The whole apparatus is explained in detail so an accurate computer model can be made. Several simulation approaches are given, and all prove the applicability in teaching coupled problems using laboratory experiments and computer modeling.

The next very interesting paper is "Determination of Cumulative Distribution Function of the Crest Value of the Lightning Current Flowing through Line Surge Arresters". For the selection and design of line surge arresters (LSA), it is essential to know the characteristics of the lightning current circulating through LSA. When lightning strikes a transmission line, only a part of the lightning current circulates through LSA. The paper also presents the calculation results of the cumulative distribution function of the lightning current circulating through arresters for particular 110 kV transmission line located in an area with high lightning activity

The third paper is "Railway system impact on voltage quality at the level of the Croatian transmission network". The paper gives a short theoretical description of the harmonic distortion and the voltage unbalance as well as the results of the voltage quality measurement. Moreover, the paper shows the impact of the railway system on the transmission network in the case that the facilities are connected to the 110 kV voltage level.

The last paper is "Peak plant models in the Electric Power System model of reliability and availability". The paper includes a general model of a peak load power plant, but also complex models, an extended model that distinguishes between peak plants and start-up failures at the start and during operation, and the model of the peak load plant with the possible postponement of exit from the operation. The paper also gives analyze of the impact on the status and indicators of the availability and reliability of the power system.

This year we are going to work on some special issues from different scientific conferences, and we hope the authors will recognize the quality of publishing works in this journal, which is definitely going to contribute to quality maintenance, but also to the improvement of the journal's quality, which is in the interest of our wide academic community.

Goran Slipac
Editor-in-Chief

Martin Dadić
martin.dadic@fer.hr

University of Zagreb
Faculty of Electrical Engineering and Computing
Unska 3, 10 000 Zagreb, Croatia

Tomislav Župan
tzupan@koncar-institut.hr

KONČAR - Electrical Engineering Institute, Inc,
Transformer Department, R&D Section,
Fallerovo šetalište 22, 10000 Zagreb, Croatia

Teaching Magneto-Thermal Coupling Using Thomson's Levitating Ring Experiment

SUMMARY

The levitating ring experiment is presented as a method for teaching magneto-thermal interactions. The complete electromagnetic model of a problem is given, together with the insight in thermal analysis. The factors for determining the vertical displacements are explained, and an elegant method for indirect measurement of induced current in the ring is introduced. The whole apparatus is explained in detail so an accurate computer model can be made. Several simulation approaches are given, and all prove the applicability in teaching coupled problems using laboratory experiments and computer modeling.

KEYWORDS

magnetic levitation, electromagnetic forces, electrodynamics

INTRODUCTION

Thomson's levitating ring is a standard demonstration in teaching undergraduate physics, which explains Faraday's and Lenz laws, as well as the forces on the current-carrying conductor in magnetic field. It was shown initially in 1887 by Elihu Thomson as a launching ring experiment, and in 1890 John A. Fleming demonstrated a levitating variant, which is widely used in teaching electrodynamic theory [1],[2]. Due to a nonlinear character of the device, it is also used in teaching control systems, either using nonlinear models [3]-[5] or linear ones [6]-[11]. There are also papers describing the control systems for magnetic suspension [2],[12]-[15], which is another approach to the levitation experiments. In control-systems environment, the device is often modeled using the black-box approach, or only the parameters needed for the control systems synthesis (like excitation coil inductance) are calculated using the electromagnetic theory. In general physics, the underlying electromagnetic phenomena are often oversimplified [16].

At all universities, courses in undergraduate electromagnetic theory usually have some kind of a laboratory. With the wide spreading of numerical analysis software, it is tempting to include them in the student's laboratory. At many universities the whole laboratory is based only on the finite element (FEM) simulation, and at some other the laboratory is based solely on the experiments.

The main purpose of this paper is to describe a successful application of the levitating ring experiment in such a laboratory, where the experiments are linked with the coupled electromagnetic and thermal FEM simulation. A real experiment helps the students to better understand the purpose, limits and the application areas of numerical analysis software, and to better visualize object and phenomena that they are modeling.

In addition, all the elements of the experiments are carefully analyzed and thoroughly explained from the engineer's point of view, and an elegant way to indirectly measure the current in the ring is described.

In application, some of the measurements or calculations may be omitted and the guidelines for such modifications are given in the paper. With all presented elements, the experiment can be also applied in a laboratory of undergraduate electromechanics.

The paper is organized as follows: in Section II the analytical electromagnetic model is given. Section III presents the laboratory model and Section IV explains the factors contributing to the elevation of the ring. The thermal analysis is given in Section V. Section VI introduces the method for indirectly measuring the induced current in the ring. Finally, results of measurements and computer simulations are given in Sections VII and VIII, respectively.

ANALYTICAL ELECTROMAGNETIC MODEL

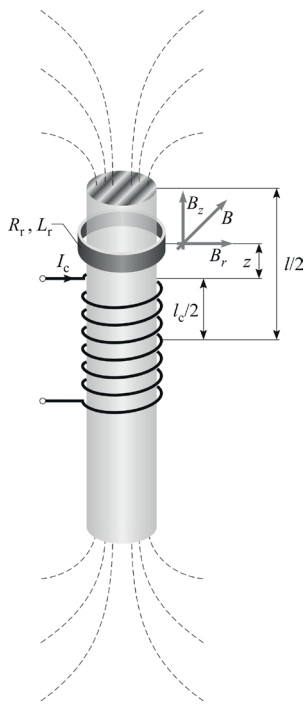


Fig. 1. Working principle of the levitating ring apparatus

The apparatus consists of a copper coil circularly wound around the laminated ferromagnetic core. The core protrudes upwards out of the coil to guide the ring. The ring, made out of non-magnetic conducting material (copper or aluminum) is stacked on the core and initially lies reclined to the coil. If we connect the coil to a proper sinusoidal voltage source, the ring starts to levitate at the height determined by the amount of current flowing through the coil.

The working principle of the described device is explained in [10], [17] and shown in Fig. 1. Current flowing through the coil will create the magnetic field. Magnetic field lines inside the core will roughly be parallel with the core axis. Outside the core, they will form closed curved lines. Therefore, in each position of the ring, the coil's magnetic field will have both axial B_z and radial B_r components, which we can express in cylindrical coordinate system as

$$\vec{B}_z = B_{z0} \sin(\omega t) \vec{a}_z, \quad (1)$$

$$\vec{B}_r = B_{r0} \sin(\omega t) \vec{a}_r. \quad (2)$$

Here, B_{z0} and B_{r0} represent the peak axial and radial magnetic flux densities, ω represents the angular frequency $\omega = 2\pi f$, where f is the frequency of the sinusoidal source, t represents time and \vec{a}_z and \vec{a}_r stand for axial and radial unit vectors, respectively.

The induced electric field around the perimeter of the ring is related with the axial component of the magnetic flux density B_z . Assuming that the magnetic flux density throughout the surface of the ring's cross section is uniform and that the ring thickness is negligible, we obtain the induced electric field using the Faraday's law of electromagnetic induction:

$$\nabla \times \vec{E} = -\frac{\partial B}{\partial t}, \quad (3)$$

$$\vec{E}(b, t) = -\frac{\omega b B_{z0}}{2} \cos(\omega t) \vec{a}_\alpha, \quad (4)$$

where b is the radius of the ring. Now we can calculate the induced voltage in the ring, using

$$e = \oint \vec{E} \cdot d\vec{l} = -\omega \pi b^2 B_{z0} \cos(\omega t). \quad (5)$$

If the impedance of the ring is $Z_r = \sqrt{R_r^2 + (\omega L_r)^2}$, where R_r and L_r represent ring's resistance and inductance, respectively, the induced current in the ring will be

$$i_r = \frac{e}{Z_r} = -\frac{\omega \pi b^2 B_{z0}}{Z_r} \cos(\omega t - \varphi_r) = I_{r0} \cos(\omega t - \varphi_r). \quad (6)$$

Here, φ_r is the ring's impedance phase angle:

$$\varphi_r = \arctan \frac{\omega L_r}{R_r}. \quad (7)$$

If the ring is placed in a magnetic field with magnetic flux density \vec{B} , the force acting on an infinitesimal segment $d\vec{l}$ of the ring is

$$d\vec{F} = i_r d\vec{l} \times \vec{B}. \quad (8)$$

Therefore, the total force on the ring is equal to

$$F = i_r 2\pi b B_{r0} \sin(\omega t). \quad (9)$$

As can be seen, only the radial component of the magnetic flux density affects the axial force which causes the levitation of the ring. The field's axial component causes the radial force on the ring and integrating it over the ring's perimeter the result is zero (if the ring is placed horizontally). Obviously, this manifests as the radial stress on the ring, trying to compress it inwards, towards its axis. As can be seen in (9), the force is time-varying. Therefore, its average value is significant when calculating the axial displacement of the ring:

$$F_{avg} = 2\pi b I_{r0} B_{r0} \frac{1}{2\pi/\omega} \int_0^{2\pi/\omega} \cos(\omega t - \varphi_r) \sin(\omega t) dt = \pi b I_{r0} B_{r0} \sin \varphi_r. \quad (10)$$

If m is the mass of the ring, g the gravitational acceleration, c the viscous damping coefficient and x the elevation of the ring, the motion equation can be written as

$$m \frac{d^2 x}{dt^2} + c \frac{dx}{dt} = F(x) - m g. \quad (11)$$

The gravitational pull opposes the electromagnetic force and, after the initial transient movement, the ring levitates at the point where these two forces cancel each other.

In reality, the magnetic flux density and its radial and axial components cannot be calculated analytically. The same holds for the inductance, and the problem is even more complicated with the thermal dependence of the ring's resistance. Increasing the current in the ring, it dissipates more power which causes it to warm up and thus its resistance increases. Consequently, the increased resistance lowers the current and the force, causing the ring to gradually "sink" until a stable working point is reached. The whole process of heat dissipation is also calculable only using numerical methods, and since two processes (magnetic and thermal) are coupled it is tempting to apply coupled numerical analysis. In addition, with the finite dimensions of the ring, the lumped-parameter calculation becomes inaccurate both for electromagnetic and thermal calculation.

LABORATORY MODEL

The coil is made out of 576 turns of copper wire (0.95 mm in diameter) circularly wound in a hollow cylinder form with 18.6 and 31.8 mm inner and outer diameter, respectively. The core is made out of laminated non-oriented electrical steel, assembled out of 30 sheets. Because of the easier assembling, it's cross section is rectangular (9.85 mm x 10.1 mm) with overall height equal to 200 mm. Paper ruler is attached to one side of the core for measuring the height of the levitating ring. The detailed layout of the model, together with the dimensions, is visible in Fig. 2.

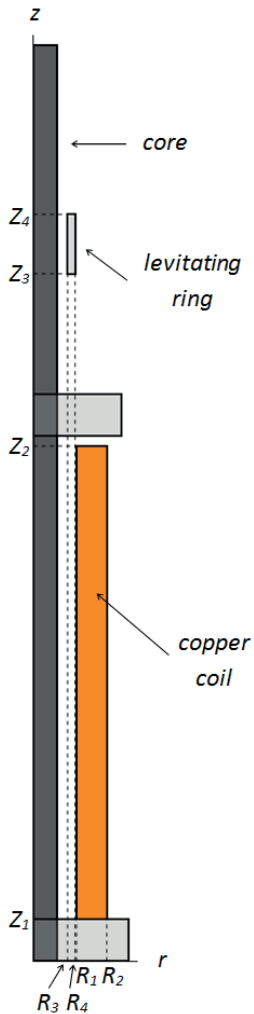


Fig. 2. Side view of the apparatus. Coil parameters are $R_1=9.3$ mm, $R_2=15.9$ mm, $Z_1=9.15$ mm, $Z_2=112.45$ mm. Ring parameters are $R_3=7.375$ mm, $R_4=9$ mm, $Z_3=Z_4=13$ mm. Core parameters are (W x D x H) $10.1 \times 9.85 \times 200$ mm

TABLE I
ALUMINUM ALLOY 5005-O PHYSICAL, ELECTRICAL AND THERMAL PROPERTIES [17]

Property	Value
density	2.70 g/cm ³
electrical resistivity	3.32 x 10 ⁻⁸ Ωm
temperature coefficient	0.0036 K ⁻¹
specific heat capacity	0.900 J/g°C
thermal conductivity	200 W/mK



Fig. 3. Levitating ring apparatus.

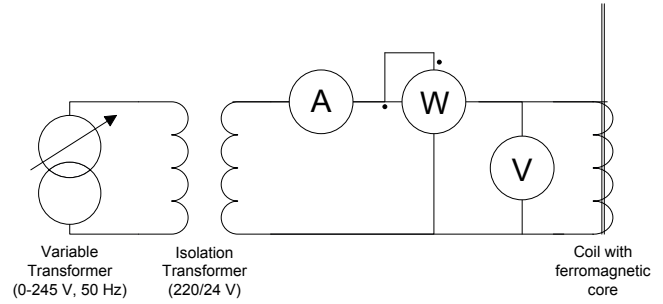


Fig. 4. Connection diagram of the levitating ring apparatus.

The ring is made out of aluminum alloy 5005-O, whose physical, electrical and thermal properties are given in Table I [18]. It is 13 mm high with the inner and the outer radius equal to 7.375 mm and 9 mm, respectively. For the sinusoidal voltage-regulating source, Iskra MA 4803 variable transformer was used (245 V, 50 Hz). It is connected to the isolation transformer (220/24 V) in order to ensure the safety of non-professionals (e.g. students) using the levitating ring apparatus. Two true RMS digital multimeters (UNI-T UT60E) are used for measuring the voltage of the coil and the current flowing through it. For measuring the electric power of the coil, Iskra OES0101 digital wattmeter is used (accuracy class of 0.1 at the 40-60 frequency range). Finally, FLIR i7 thermal camera is used in order to accurately measure the temperature of the ring. Since the emissivity of the polished aluminum is 0.04-0.06 [19], a standard black electrical tape was cut in a square 4 mm wide and attached to the ring. The emissivity of such a tape is 0.96 and therefore the temperature of the ring can be precisely measured using the thermal camera. Whole apparatus demonstrating the levitating ring experiment is visible in Fig. 3 and the connection diagram in Fig 4.

HEIGHT OF THE RING AND ITS VERTICAL DISPLACEMENT

In [17] the influence of the phase angle of the ring's impedance on the vertical displacement is presented. Nevertheless, the influence of the ring's height on the phase angle is only briefly elaborated. In [10] the inductance of the ring is calculated for a circular ring. In this section, an engineering perspective will be given to the calculation of the inductance of the applied ring, which was in the form of a hollow cylinder.

The alternating current flowing through the coil induces the electromagnetic force which pulls the ring upwards. Equation (10) shows that three main parameters dictate the value of the force: the induced current flowing through the ring I_{r0} , the radial component of the magnetic flux density B_{r0} and the ratio of the ring's inductance over its resistance $\sin \varphi_r$ (see (7)). These three parameters and their influence on the elevation of the levitating ring are explained next.

The electromagnetic force will decrease with the elevation, since the magnetic flux density decreases with distance from the coil [20]. The ring will levitate at the point where that force is equal to the gravitational pull on the ring.

In order to calculate the factor $\sin \varphi_r$, the inductance and the resistance of the ring have to be obtained. Since the ring used in the experiment has the shape of a hollow cylinder, the resistance can be calculated using the thin-wall solenoid approximation

$$R_r = \rho \frac{l}{A} \quad (12)$$

Here, ρ is the electrical resistance of the material of the ring, l is the mean circumference of the ring and A is the area of the cross section of the ring. We obtain

$$R_r = \frac{\rho \pi}{h} \cdot \frac{b_o + b_i}{b_o - b_i} \quad (13)$$

where h is the height of the ring and b_o and b_i represent the outer and the inner radius of the ring, as visible in Fig. 5.

The calculation of the inductance of the circular ring with rectangular cross section is not trivial. Since the ring in this experiment is relatively thin, the same thin-wall solenoid approximation can be used. Self inductance can then be obtained using [21]

$$L_r = \frac{4\mu_0 b_{mean}^2}{3h\beta k^3} \left((2k^2 - 1)E(k) + (1 - k^2)K(k) - k^3 \right). \quad (14)$$

Here, μ_0 is the permeability of air, b_{mean} is the ring's mean radius ($b_{mean} = \frac{b_o + b_i}{2}$) and $E(k)$ and $K(k)$ are the complete elliptic integrals of the first and the second kind. Factors β and k are calculated as follows:

$$\beta = \frac{h}{2b_{mean}}, \quad (15)$$

$$k = \sqrt{\frac{1}{1 + \beta}}. \quad (16)$$

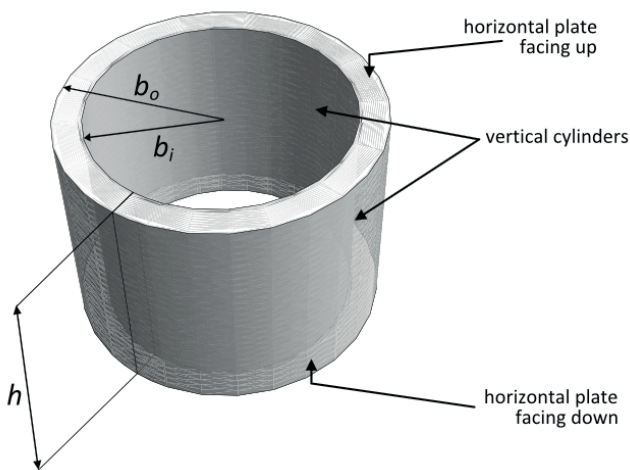


Fig. 5. Aluminum ring in the form of a hollow cylinder.

TABLE II
STEADY-STATE ELEVATION OF DIFFERENT RINGS
($I_{coil}=1.5$ A, INNER AND OUTER RADIUS ARE THE SAME FOR ALL THREE RINGS)

Ring's height (mm)	Elevation (mm)
3.1	4
6.3	29
13	52

Fig. 6 shows the correlation of the ratio of the ring's inductance over its resistance with regards to the height of the ring. It is clearly visible that the ratio increases, i.e. the character of the ring's impedance is increasingly inductive. Consequently, the parameter $\sin \varphi_r$ in (10) increases which means that the ring with greater height can achieve higher vertical displacement from the coil (its levitating point is higher). Using the laboratory model from Section III, the steady-state elevation of three rings with different heights is presented in Table II.

The induced current flowing through the ring I_{r0} , according to (6), is determined by the source frequency, axial component of the magnetic flux density, ring's radius and the impedance of the ring. Since the resistance of the ring is very low, the induced current tends to be relatively high. If the ring is kept levitating for a relatively long period of time, the ring's temperature will noticeably increase. Consequently, increasing the ring's temperature, its resistance increases as well, according to the linear approximation of temperature dependence

$$R_{r,g} = R_r \left(1 + \alpha (\vartheta - 20^\circ \text{C}) \right), \quad (17)$$

where ϑ is the temperature in the Celsius temperature scale, α is the temperature coefficient of the material of the ring, R_r is the ring's resist-

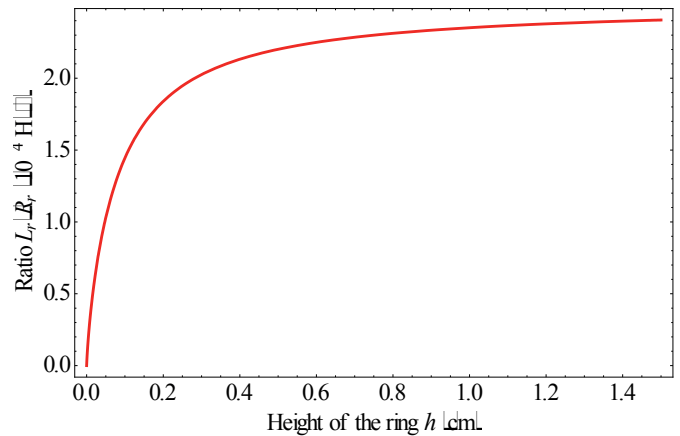


Fig. 6. Correlation of the ratio of the ring's inductance over its resistance with regards to the height of the ring. The geometry of the ring and its electrical resistivity is given in Fig. 2 and Table I.

TABLE III
PROPERTIES OF AIR [22]
(AT ATMOSPHERIC PRESSURE OF 101.3 kPa AND TEMPERATURE OF 300 K)

Symbol	Property	Value
g	gravitational acceleration	9.80665 m/s ²
β	thermal expansion coefficient (for air $\beta=1/T_\infty$)	0.0033 K ⁻¹
ν	kinematic viscosity	15.68 x 10 ⁻⁶ m ² /s
α	thermal diffusivity	22.16 x 10 ⁻⁶ m ² /s
k	thermal conductivity	0.02624 W/m K
ρ	density	1.177 kg/m ³
c_p	specific heat capacity	1005.7 J/kg K
Pr	Prandtl number	0.708

ance at 20°C and $R_{r,g}$ is the ring's resistance at the temperature ϑ . The increased resistance of the ring will cause the current flowing through it to decrease and hence the overall electromagnetic force exerted on the ring will decrease. As a consequence, the ring will slowly "sink" (its elevation will gradually fall) as the ring's temperature increases.

As can be seen from the abovementioned, the behavior of the levitating ring cannot be easily predicted or calculated. This justifies the usage of the levitating ring experiment in teaching control systems as described in the Section I. The number of overlapping physical effects makes this experiment well suitable in teaching engineering electrodynamics and electromagnetically and thermally coupled-problem solving, as well.

THERMAL ANALYSIS

Previous chapter explained the influence of the increased temperature of the ring on its elevation height. If the alternating source in the experiment apparatus is turned on for a long period of time, the levitating ring will finally come to a steady state and its elevation height will not further decrease with time. At that point the heat generated in the ring due to the power loss (Joule heating) will become equal to the heat dissipated from the ring to its surroundings. The mechanisms explaining the heat exchange are complicated and involve solving the convective heat transfer and the thermal

radiation equations. However, by neglecting or approximating some thermal effects, the thermal model of the ring may be analytically explained.

If a hot object is radiating energy to its cooler surroundings, the radiation heat loss rate can be expressed as

$$\dot{q}_{rad} = \varepsilon\sigma(T_s^4 - T_\infty^4)A, \quad (18)$$

where ε is the emissivity of the object, σ is the Stefan-Boltzmann constant ($\sigma = 5.6703 \cdot 10^{-8} \text{ W/m}^2\text{K}^4$), T_s is the surface temperature of an hot object (absolute, thermodynamic temperature in K), T_∞ is the temperature of the surroundings (also in K) and A is the area of the object. Since the ring in this experiment is made out of highly polished aluminum whose emissivity is around 0.04 [22], the heat dissipation by radiation can be neglected.

The convective heat transfer caused by the movement of the heated air around the levitating ring can be approximated using the analytical expressions for natural convection on vertical cylinders and on horizontal plates. The Newton's law of cooling states that the rate of convection heat transfer \dot{q}_{conv} is

$$\dot{q}_{conv} = \frac{dQ}{dt} = h \cdot A(T_s - T_\infty), \quad (19)$$

where Q is the thermal energy (in joules), h is the convection heat transfer coefficient ($\text{W/m}^2\text{K}$), A is the surface area of the heat being transferred (m^2), T_s is the temperature of the object's surface (in K) and T_∞ is the temperature of the environment (in K).

The heat transfer coefficient h is characterized by the geometry of the object, its physical properties and the positioning in the environment. The four surfaces of the cylindrical ring, due to its sharp edges, can be approximated with the horizontal plate facing up, the horizontal plate facing down and two vertical cylinders, as illustrated in Fig. 5. The coefficient h is defined as

$$h = \frac{Nu \cdot k}{L}, \quad (20)$$

where Nu is the Nusselt number, k is the thermal conductivity of the material and L is the characteristic length of the surface. In order to calculate the Nusselt number, the Rayleigh number has to be defined as well:

$$Ra_L = \frac{g\beta}{\nu\alpha}(T_s - T_\infty)L^3. \quad (21)$$

All the parameters are defined in Table III. If, for the sake of simplicity, the air flow is assumed to be laminar, the Nusselt number for a horizontal plate facing up is [23]

$$Nu = \frac{1.4}{\ln\left(1 + \frac{1.4}{0.835 C_{lam} Ra_L^{0.25}}\right)}. \quad (22)$$

The coefficient C_{lam} is defined as

$$C_{lam} = \frac{0.671}{\left(1 + \left(\frac{0.492}{Pr}\right)^{9/16}\right)^{4/9}}, \quad (23)$$

where Pr is the Prandtl number (Table III). The characteristic length is equal to the ratio of the plate surface area to its perimeter, which in this case is equal to

$$L = \frac{area}{perimeter} = \frac{(b_o^2 - b_i^2)\pi}{2\pi(b_o + b_i)} = \frac{b_o - b_i}{2}. \quad (24)$$

The Nusselt number for a horizontal plate facing down is equal to [23]

$$Nu = \frac{2.5}{\ln\left(1 + \frac{2.5}{0.527 Ra_L^{0.2}} \left(1 + \left(\frac{1.9}{Pr}\right)^{0.9}\right)^{2/9}\right)}. \quad (25)$$

The characteristic length is given in (24). Finally, the Nusselt number for a vertical cylinder is [23]

$$Nu = Nu_{vp} \frac{\xi}{\ln(1 + \xi)}, \quad (26)$$

where Nu_{vp} is the Nusselt number for a vertical flat plate (i.e. neglecting the curvature of the cylinder),

$$Nu_{vp} = \frac{2.0}{\ln\left(1 + \frac{2.0}{C_{lam} Ra_L^{0.25}}\right)}. \quad (27)$$

Here, C_{lam} is given in (23), and the characteristic length L is equal to the height of the plate (the height of the cylinder in this case). Factor ξ takes into account the influence of the curvature and is defined as

$$\xi = \frac{1.8}{Nu_{vp}} \frac{L}{D}, \quad (28)$$

where D is the diameter of the cylinder.

Knowing the temperatures of the environment and of the object, using (18)-(28) the total heat transfer of the cylindrically shaped object can be calculated. However, since the dimensions of the ring are relatively small, the analytical equations given yield inaccurate results. Therefore, numerical methods with a more detailed approach should be used when trying to accurately model the thermal characteristics of the ring. The above-mentioned parameters are explained in order to become acquainted with the thermal analysis nomenclature and to have a more insight when simulating this experiment using a computer. There is a plenty of available literature with a more detailed approach to heat transfer theory and computational thermal analysis [22-26].

INDIRECT MEASUREMENT OF THE CURRENT IN THE RING

None of the papers dealing with the levitating ring experiment [1]-[16] present the method for measuring or calculating the induced current in the ring. One of the approaches would be to make an accurate thermal model of the ring. Since all the heat generated inside the ring comes from the Joule losses, the current can be obtained knowing the heat transfer from the ring to its surroundings. This can only be accurately achieved using the computational thermal analysis, which is out of scope of many electrical engineers. This section presents an indirect way of measuring the Joule losses. Thus, the induced current in the ring can be calculated more precisely.

If we connect the apparatus according to the connection diagram in Fig. 4, the real power measured will consist of Joule losses in the coil, hysteresis and eddy current losses in the ferromagnetic core and the Joule losses in the aluminum ring. The ferromagnetic core is laminated which minimizes the core losses caused by the eddy currents. If the core is made out of the low-loss material, the hysteresis losses will be significantly smaller in comparison with the coil losses. Furthermore, because of the open-core type, these losses will be reduced even more since the magnetic flux density inside the ferromagnetic core is low.

Keeping the current in the coil equal throughout the measurements, if P_{w2} is the measured real power with the levitating ring inserted and the P_{w1} without it, we can determine the Joule losses in the aluminum ring as the difference in measurements

$$P_{w2} - P_{w1} = I_r^2 R_{rg}, \quad (29)$$

where $I_r = I_{r0}/\sqrt{2}$ is the effective value of the induced current in the ring. Using (17) and knowing the geometric and electrical properties of the ring together with its temperature, the current flowing through the ring is

$$I_r = \sqrt{\frac{P_{w2} - P_{w1}}{R_{r,g}}} \quad (30)$$

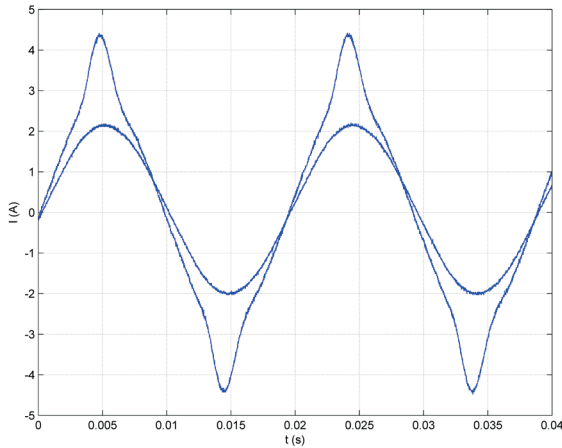


Fig. 7. Measured waveforms of the excitation currents in the coil. At 1.5 A (RMS) the waveform is sinusoidal and at 2 A (RMS) the waveform is distorted due to the core's nonlinearity.

Excitation current in the coil has to be sinusoidal for the digital wattmeter used to be accurate. Therefore, we have to be in the linear part of the B - H curve of the ferromagnetic material of the core (i.e. the relative magnetic permeability of the material has to be constant). Fig. 7 shows the oscilloscope waveforms of the excitation currents at 1.5 A (RMS) which is practically sinusoidal, and at 2 A (RMS) where the nonlinearity of the core becomes apparent.

MEASUREMENTS

The measurements were done on apparatus explained in Section III. The excitation current in the coil was targeted at 1 A (RMS) and 1.5 A (RMS) and two sets of measurements were taken within a time frame of 10 minutes with the time step of 0.5 minute. Prior to the measurements and the insertion of the ring, the current through the coil was flowing long enough for the coil to reach a steady temperature. The elevation of the aluminum ring was measured at the upper side of the ring using the attached paper ruler, as visible in Fig. 3. The temperature readings were obtained using the thermal camera. The temperature of the surroundings was 28.6 °C and 29.0 °C and the real power of the coil without the ring inserted was $P_{w1}=3.05$ W and $P_{w1}=1.45$ W for the first and the second set, respectively.

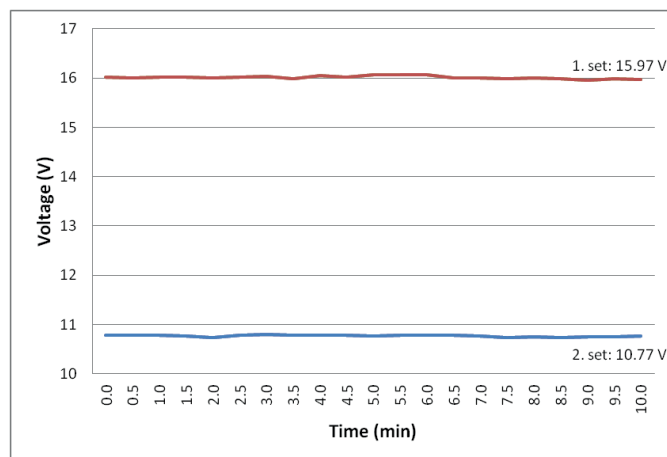


Fig. 8. Voltage of the coil remained unchanged in time for both sets of measurements.

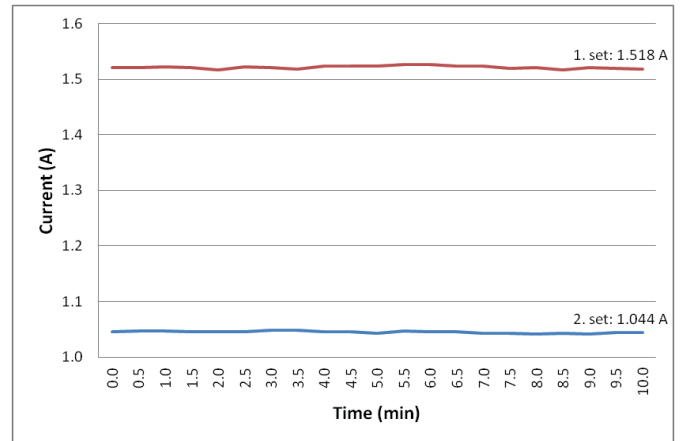


Fig. 9. Current inside the coil remained unchanged in time for both sets of measurements.

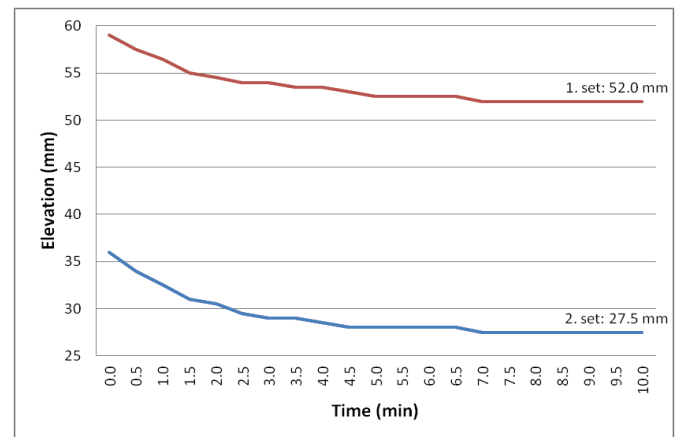


Fig. 10. Elevation of the ring gradually decreased in time until a steady state was achieved.

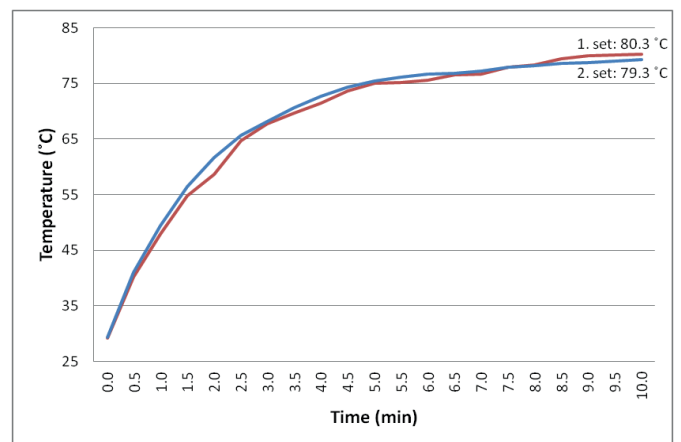


Fig. 11. Temperature of the ring increased in time.

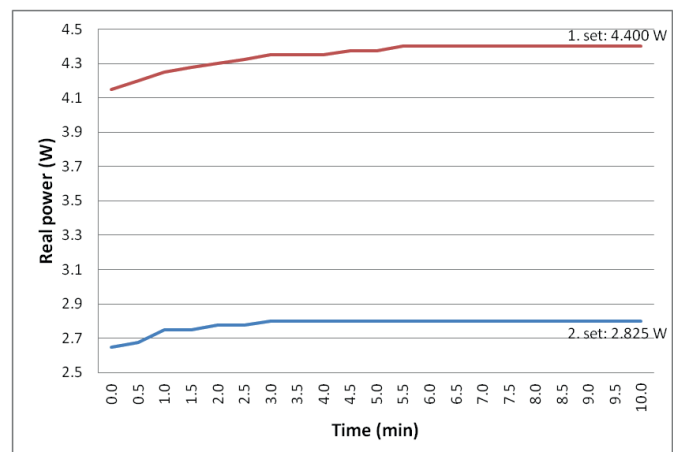


Fig. 12. Real power of the coil gradually increased in time until a steady state was achieved.

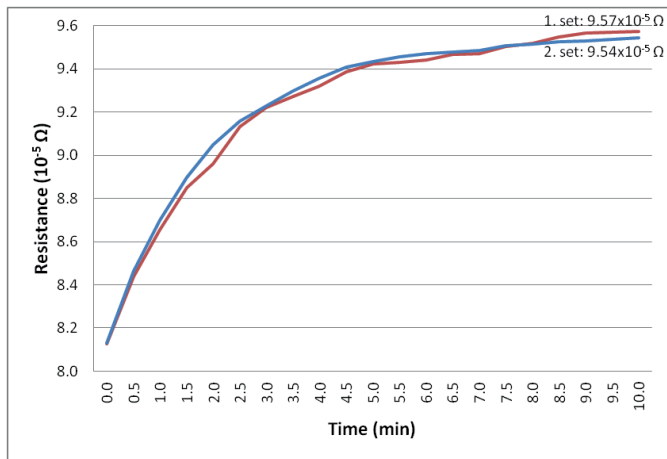


Fig. 13. Calculated resistance of the ring as a function of time.

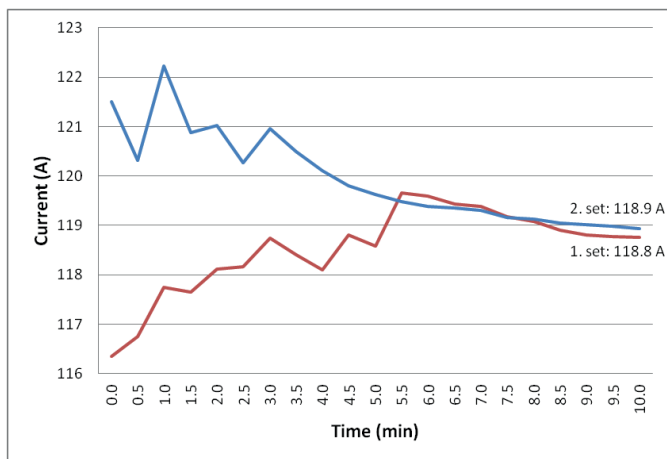


Fig. 14. Calculated current flowing through the ring as a function of time.

The voltage and the current of the coil remained unchanged throughout the measurements, as can be seen in Fig. 8-9. All the other measured parameters (elevation, temperature, real power) change until the steady state is achieved, as is visible in Fig. 10-12. Finally, Fig. 13 shows the calculated resistance of the ring using (17) and Fig. 14 the calculated current flowing through the ring using (30).

A number of conclusions can be deduced from the presented figures. If the voltage and the current of the coil remain unchanged (Fig. 8-9) and the overall real power gradually increases until a steady state is achieved (Fig. 12), obviously the power factor increases as well. This means that the phase angle between the voltage and the current decreases, i.e. the character of the impedance of the load becomes more and more resistive. The ring will levitate at the position where the magnetic force acting on it equals its own weight, as explained in Section II. Since the temperature of the ring rises (Fig. 11), its resistance rises as well (Fig. 13), meaning that the current flowing inside it should decrease. The magnetic force is now lower and it cannot compensate the pull of the ring's weight and the ring moves downwards. Now the ring is closer to the coil and the axial magnetic flux density increases which leads to the increased induced voltage in the ring (5). This increases the current in the ring and the magnetic force-weight equilibrium is achieved again. The calculated current flowing through the ring (Fig. 14) shows that, throughout the measurements, its value remains relatively constant.

COMPUTER SIMULATIONS

Described experiment of the levitating ring can be easily simulated on a computer using one of the available FEM electromagnetic/thermal software packages. The time needed to model it is relatively low which makes it ideal for a student computer-simulations project.

To completely model the levitating ring experiment, a transient analysis, which can deal with the gradual heating and "sinking" of the ring, should be made. However, the complexity of such an approach makes it appropriate only for senior-year student assignments. For an undergraduate level, another approach may be applicable. Doing the measurements first, final steady state values can be used as simulation parameters. Using Fig. 10, the ring can be placed at the proper elevation and applying the measured currents (Fig. 9) the magnetic force and current in the ring can be obtained. Also, if a coupled electromagnetic-thermal analysis is done, the final temperature of the ring can also be retrieved.

The simulations in this paper are done using the *Infolytica MagNet* and *ThermNet* software. Depending on the software licenses available at the certain universities, there are many approaches at computer modeling of the levitating ring experiment, as presented in the next subsections.

A. 3D Electromagnetic-Thermal Coupled Simulation

The levitating ring apparatus can be modeled using the geometric, electrical and physical properties from the Section III. A custom material is specified for the ring using the Table I. For the ferromagnetic core, an M270-35A non-oriented fully processed electrical steel is chosen based on the thickness and core losses [27]. Finally, a 98% IACS copper is used for modeling the coil. All the plastic protrusions and supports are omitted from the model since they do not affect its electromagnetic properties. Obviously, the teachers should choose the materials appropriate for their available equipment when setting up this project. For the thermal part of the simulation, only the ring is taken into consideration for the sake of simplicity. The four surfaces are modeled according to Section V and the temperature of the surroundings is set as in the measurements.

B. 2D Electromagnetic-Thermal Coupled Simulation

If only 2D modeling software is obtainable it can be used as well and still achieve satisfactory results. Since the ring and the coil can be modeled in 2D geometry, only the ferromagnetic core with rectangular cross section has to be approximated in 2D. A standard procedure of equaling the cross section areas can be used. If a rectangular cross section needs to be transformed into a circular one, the radius of a circular cross section has to be

$$R_{circular} = \sqrt{\frac{width \times depth}{\pi}}, \quad (31)$$

which, in this case, using the data from Fig. 2, yields $R_{circular} = 5.62735$ mm.

Obviously, the 2D approach can be used without the abovementioned approximation if a laboratory model is made with ferromagnetic cores with circular cross section.

C) 3D or 2D Electromagnetic Simulation

For a pure electromagnetic analysis, the thermal calculation can be omitted. The problem is then simpler, since no thermal modeling needs to be done. Using the measurements (Fig. 13), the final steady state temperature of the ring has to be defined in the simulation software used in order to accurately calculate the resistance and, therefore, the induced current flowing in the ring.

D) Simulation Results

As with the measurements, the two sets of calculations were done. The results obtained using the different computer simulation approaches, together with the measured values, are presented in Tables IV-V.

The magnetic force in Tables IV-V is equaled to the calculated weight of the ring using the density from Table I and geometric parameters of the ring from Fig. 2. The total weight G of the ring calculated this way is

$$G = gm = g\gamma V = g\gamma h\pi (b_o^2 - b_i^2), \quad (32)$$

where g is the gravitational acceleration, m is the mass of the ring, V is its volume and γ is the density of the ring (Table I).

As can be seen from the calculated results, the 3D electromagnetic-thermal coupled computer simulation provides, as expected, the results

TABLE IV
MEASURED AND CALCULATED RESULTS FOR THE LEVITATING RING
 $I_c = 1.518$ A, ELEVATION OF THE RING = 52.0 MM, $T_{SURROUNDINGS} = 28.6$ °C

Approach	Induced current (A)	Magnetic force (mN)	Temperature (°C)
Measurement	118.8	28.8 ^{a)}	80.3
3D Coupled	118.5	29.0	76.9
2D Coupled	111.6	24.9	71.5
3D Electromagnetic	117.4	28.5	80.3 ^{b)}
2D Electromagnetic	108.7	23.6	80.3 ^{b)}

^{a)} Gravitational pull calculated from the geometric parameters of the ring (Fig. 2) and its density (Table I) using (31)

^{b)} Temperature defined in the simulation

TABLE V
MEASURED AND CALCULATED RESULTS FOR THE LEVITATING RING
 $I_c = 1.044$ A, ELEVATION OF THE RING = 27.5 MM, $T_{SURROUNDINGS} = 29.0$ °C

Approach	Induced current (A)	Magnetic force (mN)	Temperature (°C)
Measurement	118.9	28.8 ^{a)}	79.3
3D Coupled	119.0	28.9	77.7
2D Coupled	113.0	24.7	72.9
3D Electromagnetic	118.5	28.6	79.3 ^{b)}
2D Electromagnetic	111.0	23.9	79.3 ^{b)}

^{a)} Gravitational pull calculated from the geometric parameters of the ring (Fig. 2) and its density (Table I) using (31)

^{b)} Temperature defined in the simulation

closest to the measured values. All the other simulation approaches offer results that are still quite satisfying and prove that, if full 3D licenses are not available, the levitating ring experiment can be modeled accurately.

CONCLUSIONS

Teaching electromagnetic theory can sometimes be a challenging task due to the complex mathematics used. The topic of levitation is appealing and interesting to students and can be an effective way in teaching engineering electrodynamics. A simple levitating ring experiment, which can be easily conducted at any electromagnetic laboratory, proves to be a practical demonstration of electromagnetic-thermal processes and a great example for teaching coupled-problem solving.

Computer simulations of the mentioned experiment can be done relatively effortlessly and can be used for student projects. Results obtained from simulations are in a good correlation with measurements and can explain the advantages of using computer modeling in designing electrical devices to students. A number of the simulation approaches, depending on the available software at the university, can be used and all produce satisfying results.

This paper presents a thorough analysis of the levitating ring experiment and its computer simulations and demonstrates it as an electromagnetic-thermal coupled problem adequate in teaching undergraduate electrodynamics and computer modeling.

Acknowledgement

This paper is fully supported by Croatian Science Foundation under the project Shielding from electromagnetic fields with electrically conductive textile materials IP-2018-01-7028. The authors would like to thank Ivica Kunšt for his help in preparing the laboratory model.

REFERENCES

- [1] R. J. Hill, "Teaching electrodynamic levitation theory," *IEEE Trans. Educ.*, vol. 33, no. 4, pp. 346-354, November 1990.
- [2] M. T. Thompson, "Electrodynamic magnetic suspension—models, scaling laws, and experimental results," *IEEE Trans. Educ.*, vol. 43, no. 3, pp. 336-342, Aug. 2000.
- [3] Z.-J. Yang, Y. Fukushima, S. Kanae, and K. Wada, "Robust non-linear output-feedback control of a magnetic levitation system by K-filter approach," *IET Control Theory Appl.*, vol. 3, iss. 7, pp. 852-864, 2009.
- [4] S. A. Green and K. C. Craig, "Robust, digital, nonlinear control of magnetic-levitation systems," *J. Dyn. Sys., Meas., Control*, vol. 120, no. 4, pp. 488-495, Dec. 1998.
- [5] S.-W. Park, "System development for education and design of a nonlinear controller with on-line algorithm," *Int. J. Control. Autom.*, vol. 1, no. 2, pp. 215-221, Jun. 2003.
- [6] R. K. H. Galvão, T. Yoneyama, F. M. U. de Araújo, and R. G. Machado, "A simple technique for identifying a linearized model for a didactic magnetic levitation system," *IEEE Trans. Educ.*, vol. 46, no. 1, pp. 22-25, Feb. 2003.
- [7] T. H. Wong, "Design of a magnetic levitation control system – an undergraduate project," *IEEE Trans. Educ.*, vol. E-29, no. 4, pp. 196-200, Nov. 1986.
- [8] P. S. Shiakolas and D. Piyabongkarn, "Development of a real-time digital control system with a hardware-in-the-loop magnetic levitation device for reinforcement of controls education," *IEEE Trans. Educ.*, vol. 46, no. 1, pp. 79-87, Feb. 2003.
- [9] R. Valle, F. Neves, R. de Andrade Jr., and R. M. Stephan, "Electromagnetic levitation of a disc," *IEEE Trans. Educ.*, vol. 55, no. 2, pp. 248-254, May 2012.
- [10] N. Barry and R. Casey, "Elihu Thomson's jumping ring in a levitated closed-loop control experiment," *IEEE Trans. Educ.*, vol. 42, no. 1, pp. 72-80, Feb. 1999.
- [11] P. S. Shiakolas, S. R. Van Schenck, D. Piyabongkarn, and I. Frangeskou, "Magnetic levitation hardware-in-the-loop and MATLAB-based experiments for reinforcement of neural network control concepts," *IEEE Trans. Educ.*, vol. 47, no. 1, pp. 33-41, Feb. 2004.
- [12] J.-L. Lin, and B.-C. Tho, "Analysis and μ -based controller design for an electromagnetic suspension system," *IEEE Trans. Educ.*, vol. 41, no. 2, pp. 116-129, May 1998.
- [13] V. A. Oliveira, E. F. Costa, and J. B. Vargas, "Digital implementation of a magnetic suspension control system for laboratory experiments," *IEEE Trans. Educ.*, vol. 42, no. 4, pp. 315-322, Nov. 1999.
- [14] W. G. Hurley, and W. H. Wölfe, "Electromagnetic design of a magnetic suspension system," *IEEE Trans. Educ.*, vol. 40, no. 2, pp. 124-130, May 1997.
- [15] W. G. Hurley, and W. H. Wölfe, "PWM control of a magnetic suspension system," *IEEE Trans. Educ.*, vol. 47, no. 2, pp. 165-173, May 2004.
- [16] M. Baylie, P. J. Ford, G. P. Mathlin, and C. Palmer, "The jumping ring experiment," *Physics Education*, vol. 44, no. 1, pp. 27-32, Jan. 2009.
- [17] Župan, Tomislav; Dadić, Martin; Štith, Željko, "Fully Coupled Dynamic Model of Thomson's Levitating Ring," *IEEE Trans Magn.*, vol. 51 no. 5, pp. 8300209-1-8300209-9, May 2015.
- [18] Aluminum 5005-O, HM Wire International, Inc, 2011. Available: http://www.hmwire.com/New%20PDFs/Aluminum_5005_Information.pdf
- [19] M. A. Bramson, "Infrared radiation, a handbook for applications", Plenum Press, 1968.
- [20] J. T. Conway, "Exact solutions for the magnetic fields of axisymmetric solenoids and current distributions," *IEEE Trans. Mag.*, vol. 37, no. 4, pp. 2977-2988, Jul. 2001.
- [21] S. Babic and C. Akyel, "Improvement in calculation of the self- and mutual inductance of thin-wall solenoids and disk coils," *IEEE Trans. Mag.*, vol. 36, no. 4, pp. 1970-1975, Jul. 2000.
- [22] W. S. Janna, "Engineering heat transfer", CRC Press, 2000.
- [23] G. Nellis, and S. Klein, "Heat transfer", Cambridge University Press, 2009.
- [24] Y. A. Cengel, "Heat transfer: a practical approach", McGraw-Hill, 2002.
- [25] W. J. Minkowycz, E. M. Sparrow, J. Y. Murthy, "Handbook of numerical heat transfer", John Wiley & Sons, 2006.
- [26] M. Favre-Marinet, S. Tardu, "Convective heat transfer", John Wiley & Sons, 2009.
- [27] Electrical steel non oriented fully processed, Cogent Power Ltd, 2002. Available: http://www.sura.se/Sura/hp_products.nsf/

Goran Levačić

Croatian Transmission System Operator Ltd.,
Zagreb, Croatia

Alain Xémard

Électricité de France R&D,
Palaiseau, France

Miroslav Mesić

Stručni nadzor d.o.o.
Zagreb, Croatia

Determination of Cumulative Distribution Function of the Crest Value of the Lightning Current Flowing Through Line Surge Arresters

SUMMARY

For the selection and design of line surge arresters (LSA), it is essential to know the characteristics of the lightning current circulating through LSA. When lightning strikes a transmission line, only a part of the lightning current circulates through LSA.

This part mostly depends on the point of impact, and the characteristic of the lightning strike current. The determination of the cumulative distribution function of the lightning current circulating through arresters is presented in first part of the paper. It can be applied on transmission lines where LSAs will be installed to protect the line against the effect of atmospheric discharges.

Second part of paper presents the calculation results of the cumulative distribution function of the lightning current circulating through arresters for particular 110 kV transmission line located in an area with high lightning activity.

KEYWORDS

atmospheric discharges, line surge arresters, cumulative distribution function, lightning current, lightning strike, EMTP, LIPS.

INTRODUCTION

1.1 Line surge arresters

The main task of a transmission system operator is the establishment of an energy supply infrastructure in order to maintain security of supply with minimal costs and environmental protection. Energy transmission is performed by a transmission network including overhead lines that are exposed to a various factors from external environment. One of them is lightning strike, also known as a natural “transient” phenomenon, which can potentially be cause for outages of transmission and distribution lines.

Nowadays the lightning phenomenon is well explored and elaborated, but

is still necessary to perform a lot of research for its full understanding. Line surge arresters (LSAs) are installed on overhead transmission lines to improve its Line Lightning Performance (LLP), by reduction of the number of outages and as a consequence for increasing reliability of the entire transmission system.

1.2 Application of LSAs on 110 kV overhead transmission line Ston - Komolac

The 110 kV overhead transmission line Ston - Komolac (with interpolated SS Rudine) is a 44 km long single circuit shielded line located in the mountainous region near Dubrovnik with a high lightning activity (the keraunic level is about 70 thunder days per year). Since it was considered that this line

had a bad lightning performance [1], the Croatian Transmission System Operator (HOPS) has started a pilot project to install line surge arresters in 2007 (Figure 1a), in order to improve the overvoltage protection, lightning performance and consequently the reliability of this line. The current configuration consists of 104 LSAs installed as follows: 50 towers with 1 LSA installed in bottom phase, 24 towers with 2 LSAs installed, one in lower and one in middle phase, and 2 towers with 3 LSAs installed, one at each of the bottom, middle and top phase. In 2008, 2 real-time measurement systems (RMS) are installed on transmission line towers no. 38 and 110 in 2009. A RMSs includes the following components: a solar power supply, a controller, an acquisition unit and a communication system. RMS (Figure 1b) has a sensor for measuring the transient current flowing through the ground conductor of the top phase LSA and a specifically developed Rogowski coil that has been installed around the tower in order to measure the total lightning current flowing through it.

FORMULATION OF THE PROBLEM

It is assumed that four different types of points of impact will be considered: tower, shield wire, phase conductor and adjacent towers. The probability of having a lightning current circulating in the arrester with a crest (peak) value, higher than a given value can be determined based on the statistics of lightning strikes on the observed transmission line. Let us denote by the current circulating in the arrester that we consider, and let us characterize a lightning strike event by the following set of random variables:



a)



b)

Figure 1: a) Part of 110 kV overhead transmission line Ston - Komolac with installed LSAs, b) LSA and real-time measurement system installed on tower no. 38.

Due to the effective selection of the LSAs it is important to know the characteristics of the lightning currents circulating through LSA. The paper shows a theoretical evaluation of the crest value of the lightning current circulating in a line arrester, and the probability followed by this variable. Calculations were performed with the software EMTP-RV and LIPS (Lightning Impact on Power Systems), which is toolbox based on EMTP (DCG version) devoted to the calculation of the failure rate of apparatus due to lightning, and covers direct and induced lightning.

- I the crest value of lightning strike current;
- X the point of impact along the transmission line.

Then I_a is a function h of I and X , as follows:

$$I_a = h(I, X) \quad (1)$$

The probability of having a current circulating in the LSA higher than the value is given by the following integral estimated from equation (1):

$$P(I_a > i_0) = P(h(I, X) > i_0) = \iint_{\{h(x,i) > i_0\}} f_{(X,I)}(x, i) dx di \quad (2)$$

where $f_{(I,X)}$ is the joint probability density function of the random variables (I, X) . Let us note that $P(I_a > i_0) = 1 - F(I_a)(i_0)$, where $F(I_a)(i_0)$ is the cumulative probability distribution of I_a , that cumulative function can be calculated as follows:

$$F_{(I_a|X=j)}(\cdot) = P(I_a < i_0) = \int_0^{i_0} f_{I_a}(i) di \quad (3)$$

In order to simplify the problem, the point of impact of the lightning strikes along the line X is considered in the following part of the paper as a discrete random variable whose values are a set $\{X_j\}$. Let us note that $f_{(I_a|X=j)}(\cdot)$ is the probability density function of the lightning strike current given that the point of impact is X_j . As indicated previously, it is assumed that three different types of impacts are used (strikes on tower, shield wire and on phase conductor). $p_x(x = X_j)$ is the probability of having a lightning strike of point of impact X_j . With these variables defined, the probability from equation (2) can be expressed as follows using the Bayes' law:

$$P(I_a > i_0) = \iint_{\{h(x,i) > i_0\}} p_x(x=1) f_{I_a|X=1}(x,i) di + \iint_{\{h(x,i) > i_0\}} p_x(x=2) f_{I_a|X=2}(x,i) di + \dots + p_x(x=1) \iint_{\{h(x,i) > i_0\}} f_{I_a|X=1} di + p_x(x=2) \iint_{\{h(x,i) > i_0\}} f_{I_a|X=2} di + \dots \quad (4)$$

The cumulative distribution function (CDF) means the probability that the real variable I_a be equal or lower than value I_0 . Therefore, as the problem is formulated to have a lightning current circulating through the LSA I_a higher than the value I_0 , the complementary cumulative distribution function is used, as follows:

$$1 - F_a(i_0) = p_x(x=1)[1 - F_{I_a|X=1}(I_0)] + p_x(x=2)[1 - F_{I_a|X=2}(I_0)] + \dots \quad (5)$$

$$\text{or} \\ F_a(i_0) = p_x(x=1)[F_{I_a|X=1}(I_0)] + p_x(x=2)[F_{I_a|X=2}(I_0)] + \dots \quad (6)$$

Where $F_a(\cdot)$ is the cumulative distribution function of the crest value of the current circulating in the arrester, $F_{(I_a|X=j)}(\cdot)$ is the cumulative distribution function of the lightning current, given that the point of impact is j as presented in equation (3), and I_a is the lightning current for the point of impact j , such as $h(I_a, j) = i_0$ (see paragraph 2). The determination of the cumulative distribution function is made based on equation (6) and involves four successive steps:

- **Step 1:** determination of the probability density function of the crest value of the lightning strike current at ground level ($0 - I_{max}$);
- **Step 2:** determination of the probability of the crest current of the lightning strikes at a given point of impact along the line (based on the notion of attractive surfaces [3]);
- **Step 3:** determination of the probability of having a lightning strike impacting the different elements of the line considered $p_x(x = X_j)$;
- **Step 4:** estimation of the probability $P(I_a > i_0)$ from the previous step.

The details of this approach are presented in the next chapter.

CUMULATIVE DISTRIBUTION FUNCTION (CDF)

3.1. Step 1

In the first step, the probability density function of having a lightning strike current in the range $0 - I_{max}$, where I_{max} is the upper value of the lightning striking the ground, is determined numerically from the lightning statistics of [4],[5]. In this paper we consider only negative downward lightning strikes because they represent in Europe 90 % of the total lightning strikes. The crest value of the first strike lightning current can be considered log-normally distributed, but the parameters of the log-normal distribution presented in [5] have to be modified in order to take into account that this distribution corresponds to measurements on towers [6] and not on the ground. The general equation of the probability density function, of a lognormally distributed random variable (in this equation is the value of the lightning crest current) is:

$$f_I(\cdot) = \frac{1}{\sqrt{2\pi}\beta I} e^{-\frac{1}{2}\left(\frac{\ln(I/M)}{\beta}\right)^2} \quad (7)$$

where M is the median value, and β is the logarithmic standard deviation.

The probability for lightning striking the ground and towers are not similar because of the Electro-Geometric Model (EGM) [7]. The probability for lightning striking on ground was determined numerically, based on a Monte-Carlo method [8][9].

3.2. Step 2

In the second step, the determination of the probability of the crest current of the lightning strikes at a given point of impact along the line was performed using attractive surfaces deduced from the application of the EGM [7]. EGM concepts imply that points of impact and lightning crest currents are correlated random variables. The EGM is a technique used to calculate the average annual number of lightning striking on the different elements of an overhead line and also the attractive surfaces of the different point of impacts [11]. The EGM model we have used was a classical one and it was based on the method presented in [5], [17]. The model of Love was used. For each point of impact one can numerically obtain the conditional probability density function of the lightning crest current for a given point of impact. As illustration, Figure 2 shows a simplified application of the EGM for a given lightning current. The lightning leaders supposed to come vertically from the cloud lead to a lightning strike on the shield wire if their trajectory has an intersection with the segment (A,B), otherwise they hit earth.

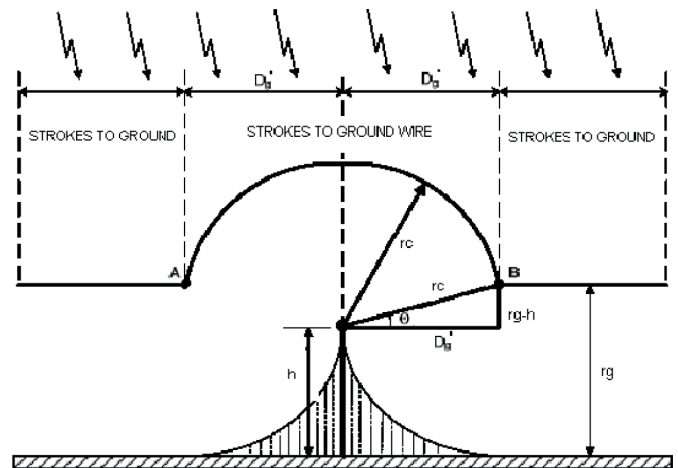


Figure 2: Electro-geometric model of a single ground wire [10].

As explained before, we have considered that the point of impact X_j is a discrete random variable with only three possible positions, considering that the line is geometrically uniform:

- tower;
- shield wire;
- phase conductor.

The conditional probability density function of the crest current at the point of impact is given by the following equation:

$$f_{I_a|X=X_j}(\cdot) = \frac{f_I(i)S(x,i)}{\int_0^\infty f_I(j)S(x,j) dj} \quad (8)$$

where f_I is the probability density function of the crest current on the ground, S is the attractive surface for the considered point of impact. S is a function of the lightning strike current and the point of impact, has been calculated in the previous step. The values of the attractive surface are taken from the EMTP-RV toolbox LIPS, according to the application of the EGM [9] for different values of I_a in the range 0-200 kA. The denominator of the right term of (8) is approximated as:

$$\int_0^\infty f_I(j)S(x,j) dj \approx \sum_0^\infty f_I(j)S(x,j) \quad (9)$$

The integral from equation (9) corresponds to the total number of lightning strikes striking , with a ground flash density equal to 1.

3.3. Step 3

As it noted in Step 2, three possible positions are considered for the point of impact: strikes to tower, shield wire and phase conductors. In order to determine the probability of having a lightning strike on the different points of impacts, some simulations with the toolbox LIPS were performed). LIPS includes a 3D EGM and is able to launch automatically EMTP-RV to calculate the flashover rate of overhead lines and the risk of failure of transmission apparatuses due to lightning [11]. LIPS's simulation results give us from the ground flash density and the structure of the line the average annual number of strikes per year and per element (tower, shield wire, phase conductors, adjacent tower). The annual number of strikes per year on the towers, adjacent to the observed tower, is taken into account, but lightning strikes on the towers and the span located after these two towers are not considered because it was proven with EMTP-RV simulations that these lightning strikes generate very low transient currents through the arresters of the observed tower. Figure 3 below shows the annual number of strikes per year on the affected elements.

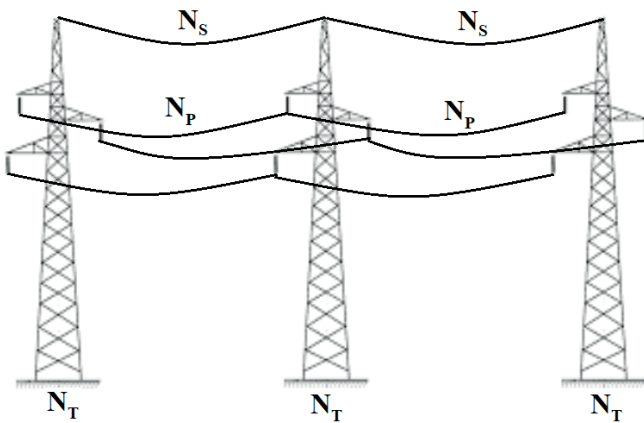


Figure 3: The annual number of strikes per year on the affected elements (tower 2 is the observed tower, tower 1 and 3 are respectively the left and right adjacent towers).

On Figure 3, N_i is the average annual number of strikes on the tower (equal for each tower), N_s is the average annual number of strikes on the shield wire (for one span) and N_p is the average annual number of strikes on the phase conductors (for one span). N_{total} is the total annual number of strikes on each element of the portion of the transmission line considered, its value can be calculated as follows:

$$N_{total} = 3N_t + 2N_s + 2N_p \quad (10)$$

The general equation for calculating the probability of having a lightning strike impacting the line on the element X_i can be calculated as follows:

$$p_x(x = X_i) = \frac{N_i}{N_{total}} \quad (11)$$

where N_i is the annual number of strikes on the stricken element of transmission line, total N is the total annual number of strikes on all the elements considered in the calculation. Consequently, the probability of having a lightning strike on the tower where the measurement system is installed can be calculated as follows:

$$p_x(x = observed_tower) = \frac{N_T}{N_{total}} \quad (12)$$

The probability of having a lightning strike on the shield wire is:

$$p_x(x = shield_wire) = \frac{2N_S}{N_{total}} \quad (13)$$

The probability of having a lightning strike on the phase conductor is:

$$p_x(x = phase_conductor) = \frac{2N_P}{N_{total}} \quad (14)$$

The probability of having a lightning strike on one adjacent tower is:

$$p_x(x = adjacent_tower) = \frac{2N_T}{N_{total}} \quad (15)$$

3.4. Step 4

In step 4, the probability of the lightning crest current $P(I_a > i_0)$, described in step 2 is estimated. Practically, for a set of values (I, X) it is possible to determine numerically with the software EMTP-RV the function h , using a limited number of simulations per point of impact considered. The modelling of the system follows the recommendations of [14], [15].

The lightning current amplitudes used in the simulations are in a range from $0-I_{max}$ (0-200 kA) in order to determine a lightning strike currents I , stroking the transmission line and leading to a current in the arrester $0-I_a$, with a crest value higher than i_0 . The simulations results were stored in a database, which allows to put into relation the values of the lightning strike currents in a range $0-I_{max}$ with the corresponding currents that circulates through the LSA in a range $0-I_{a,max}$. All parameters that are necessary to solve equation (6) are known from the previous steps, except the cumulative distribution functions $F_{I(X=j)}$, which can be estimated as follows. With a step of 1 kA, we determine the value of the lightning currents which causes a current circulating through the LSA of value I_a . Then, from the values of the lightning currents determined with the calculations performed in step 2, one selects the corresponding values of the CDF function $F_{I(X=j)}$. With this approach, all parameters that are required in order to solve equation (6) are known.

APPLICATION ON A SPECIFIC 110 kV TRANSMISSION LINE

This chapter shows the results of the calculations from step 1 to 4, for the crest value of the lightning current circulating in an arrester of the 110 kV transmission line Ston-Komolac [13]. This transmission line was chosen for calculations because route of the line is located in an area of high lightning activity and had a large annual number of outages. In order to protect against lightning, the mentioned transmission line was also equipped with LSAs, and consequently is an interesting application case of the method presented in this paper. The statistical data from [1], [2] and [12] shows how LSAs installation can significantly improve its operational reliability and its LLP. The term "observed tower", that was previously mentioned in this paper, refers to the tower where the monitoring system for measuring the lightning current circulating in arresters is installed [13].

4.1. Results of Step 1

The probability density function of the crest value of the lightning strike current on the ground level in the range $0-I_{max}$ is determined in the 1st step, which parameters are presented in Table 1. It is assumed that $0-I_{max}$ is 200 kA.

Table 1: Parameters of the log-normal distribution of the lightning current, lightning striking the ground according to [4],[5].

	< 20 kA	> 20 kA
β	1,33	0,605
M	36,2	26,2

4.2. Results of Step 2

The conditional probability density function of the lightning crest current given the point of impact as well as the attractive surfaces expressed in m^2 versus the lightning current are calculated in step 2. The calculation was performed according to equation (8). Values marked with yellow in Table 3 are expressed in percentage and mean probability density function of having a lightning strike with a crest value ; the corresponding attractive surface is indicated. For example, the density of probability that a lightning strike of 1 kA terminates on the observed tower is very low, particularly 0,00017 % with an attractive surface corresponding to this current of 100 m^2 ; the density of probability for the shield wire is 0.0059 % (with an attractive surface of 3900 m^2).

Table 2: Probability density function of the crest current at the different points of impact, and the attractive surfaces expressed in [m²] (abbreviations: t.-tower, s.w.-shielding wire and p.c.-phase conductor).

I [kA]	$S(x=t.,i)$	$S(x=s.w.,i)$	$S(x=p.c.,i)$	$f_{I X=X_i}(t.)$	$f_{I X=X_i}(s.w.)$	$f_{I X=X_i}(p.c.)$
1	100	3900	1360	0,000174	0,005937	56,072057
25	4928	18004	0	0,004354	0,292610	0
50	9740	19994	0	0,008709	0,578333	0
75	14060	20268	0	0,013063	0,834842	0
100	18096	19968	0	0,017418	1,074488	0
125	21876	19348	0	0,021772	1,298933	0
150	25376	18600	0	0,026127	1,506753	0
175	28744	17720	0	0,030481	1,706735	0
200	31896	16832	0	0,034836	1,893892	0

4.3. Results of Step 3

In 3rd step, the results are calculated with the toolbox EMTP-LIPS. These results include the annual number of strikes per year and per element (the observed tower, adjacent towers, shield wire and phase conductors).

$$p_x(x=\text{observed_tower})=0,096$$

$$p_x(x=\text{shield_wire})=0,7044$$

$$p_x(x=\text{phase_conductor})=0,0061$$

$$p_x(x=\text{adjacent_tower})=0,1929$$

The influence of both adjacent towers from the observed one is taken into account (symmetrical to the observed tower). The highest probability for lightning to strike the shield wire (70,44 %). The probability to have a lightning strike impacting the phase conductor is the lowest (0,61 %).

4.4. Results of Step 4

These results includes:

The set of values $I_a = h(I, X)$ which gives the value of the lightning strike current I , striking the transmission line at a given point of impact X , which will be at the origin of a current in the arrester of value I_a .

The set of values $F_{I|X=j}$ versus I .

The model of tower with air gaps used for EMTP-RV simulations is presented on Figure 4.

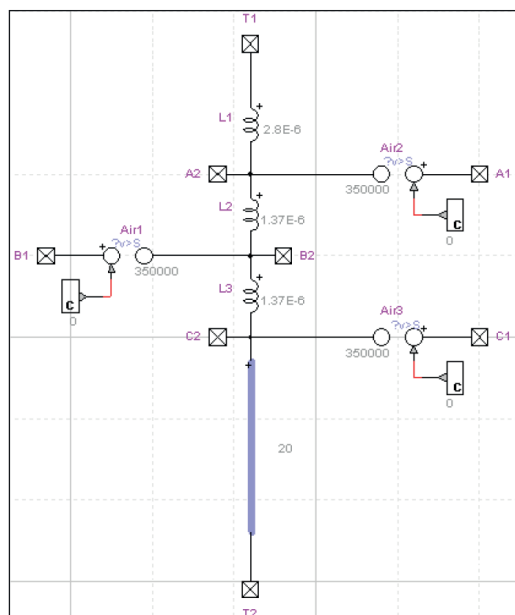


Figure 4: Model of tower with air gaps used for EMTP-RV simulations [13].

current I , striking the transmission line at a given point of impact, which causes a current in the arrester of a value I_a (it is considered that a lightning strike with higher lightning current leads to a current in the arrester higher than I_a). The set of values of the current I_a in the arrester versus the current I of a lightning strike at a given point of impact is presented below (based on data from Table 3).

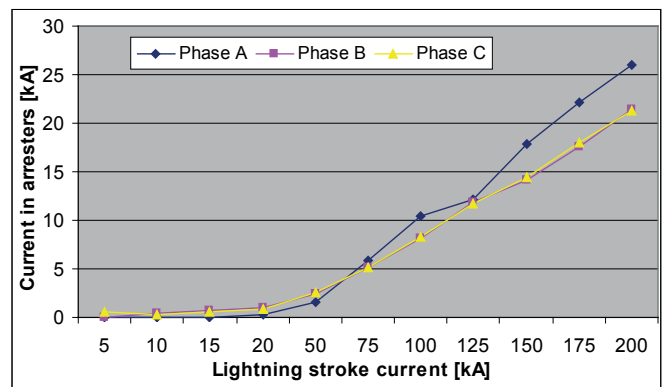


Figure 5: Current in the arrester versus lightning current for a strike at the observed tower.

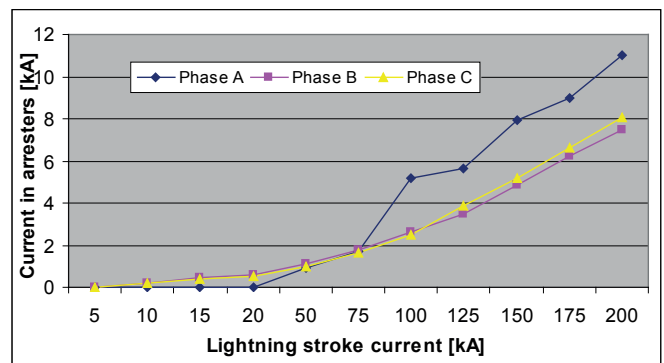


Figure 6: Current in the arrester versus lightning current for a strike at the shield wire.

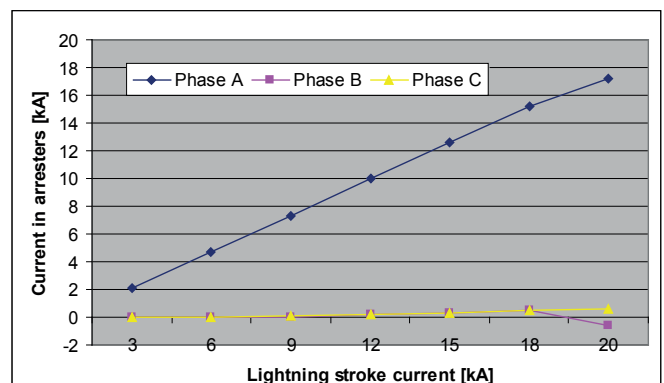


Figure 7: Current in the arrester versus lightning strike current for a lightning stroke on phase A.

Figures 5, 6, 7 and 8 present a part of the EMTP-RV simulation results. They are used for the determination of the value of the lightning strike cu-

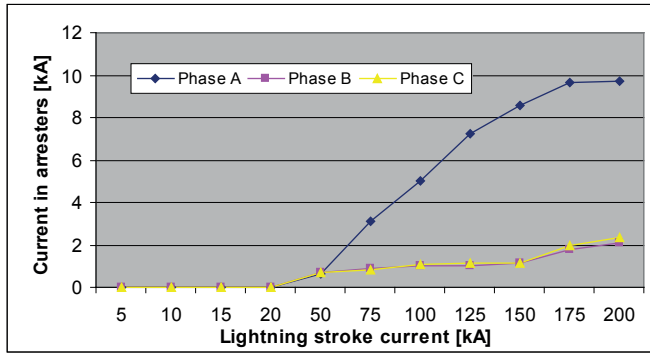


Figure 8: Current in the arrester versus lightning stroke current for a strike on an adjacent tower.

Table 3: Results of the cumulative distribution function calculated for a current circulating in the arrester in the range 0-25 kA, for different points of impact

(abbreviations: t.-tower, s.w.-shielding wire and p.c.-phase conductor, a.t.-adjacent tower).

I_a [kA]	I [kA]	F_{IX-t}	I [kA]	$F_{IX-s.w.}$	I [kA]	$F_{IX-p.c.}$	I [kA]	$F_{IX-a.t.}$
0	0	0	0	0	0	0	0	0
1	20	0,1093	50	0,8346	2	0,4109	55	0,7357
2	40	0,5306	75	0,953	4	0,8825	60	0,7824
3	60	0,7824	70	0,94	5	0,9506	73	0,8684
4	70	0,8523	85	0,9708	7	0,9987	88	0,9253
5	77	0,887	130	0,996	8	1	100	0,9521
6	80	0,8991	135	0,9965	10	1	110	0,9668
7	85	0,9164	140	0,9974	0	1	112	0,9691
8	90	0,9307	150	0,9982	0	1	144	0,9905
9	97	0,9465	175	0,9995	0	1	155	0,9938
10	100	0,9484	180	0,9996	0	1	179	0,9981
11	112	0,9691	200	1	0	1	200	1
12	125	0,9793	0	1	0	1	0	1
13	130	0,9827	0	1	0	1	0	1
14	135	0,9856	0	1	0	1	0	1
15	140	0,9889	0	1	0	1	0	1
16	145	0,9908	0	1	0	1	0	1
17	150	0,9925	0	1	0	1	0	1
18	160	0,995	0	1	0	1	0	1
19	165	0,996	0	1	0	1	0	1
20	170	0,9969	0	1	0	1	0	1
21	172	0,9972	0	1	0	1	0	1
22	175	0,9973	0	1	0	1	0	1
23	185	0,9985	0	1	0	1	0	1
24	190	0,9992	0	1	0	1	0	1
25	200	1	0	1	0	1	0	1

In Table 3, I_a is the value of current circulating in the arrester, I is the corresponding crest value of the lightning strike current and F_{IX-j} is the cumulative distribution function of the lightning current, given that the point of impact is (tower, shield wire, phase conductor and adjacent tower). Figure 10 shows (the CDF of the arrester crest current, given that lightning strikes the observed tower) that the mean value of the current is approxi-

mately about 3 kA, which means a 50 % probability considering that lightning strikes the observed tower, and causes a current circulating in the LSA higher than 3 kA. But the probability to have a current circulating in a line arrester I_a higher than 10 kA is approximately 5 %, and the probability to have a lightning current circulating in the line arrester I_a higher than 20 kA is neglectable, therefore 20 kA corresponds to the upper limit of the current circulating in the LSA, in the given case.

A part of calculation results for total CDF in the range of 0-25 kA is shown in Table 4.

Table 4: Total CDF, in the range 0-25 kA.

I [kA]	$F_a(i_a)$
0	0
1	0,7430
2	0,8697
3	0,9202
4	0,9507
5	0,9770
6	0,9814
7	0,9841
8	0,9902
9	0,9933
10	0,9944
11	0,9970
12	0,9980
13	0,9983
14	0,9986
15	0,9989
16	0,9991
17	0,9992
18	0,9995
19	0,9996
20	0,9997
21	0,9997
22	0,9997
23	0,9998
24	0,9999
25	0,9999

The CDFs of a lightning current circulating in the LSA, estimated with equation (6), taking into account the different points of impact, are shown on Figures 9-12. The analyze of figures 9 -12 leads to the following conclusions: the CDF of the current in the LSA given that lightning strikes the observed tower shows a 1% probability to lead to a transient current circulating in a LSA higher than 16 kA, while the case when lightning strikes the phase conductor A shows a 1% probability to lead to a lightning current circulating in the LSA higher than 6 kA (this is due to the protection against lightning provided by the shield wire).

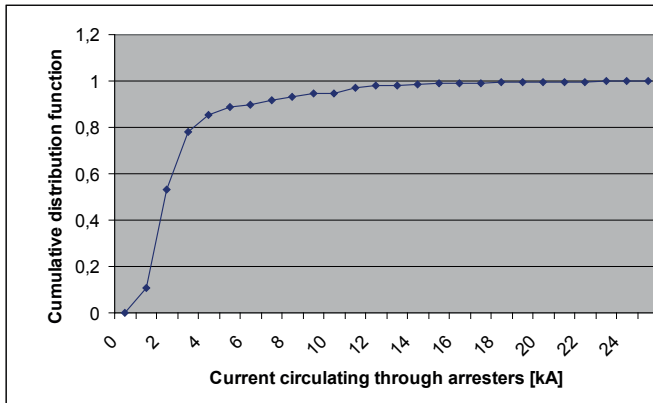


Figure 9: CDF of the current in arrester given that lightning strikes the tower where the measurement system is installed.

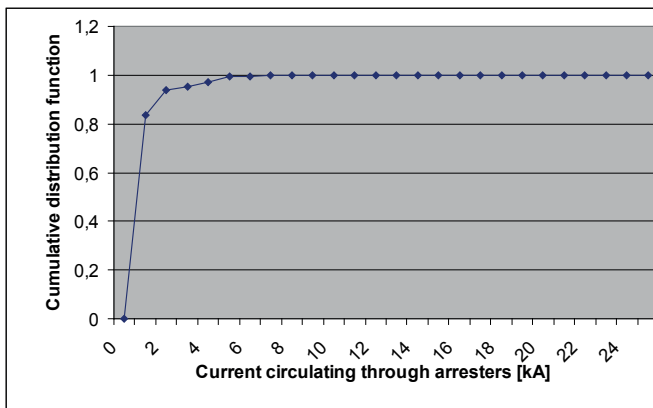


Figure 10: CDF of the current in arrester given that lightning strikes the shield wire.

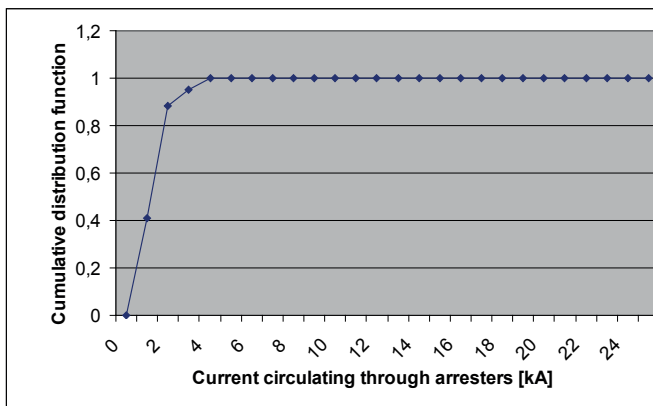


Figure 11: CDF of the current in arrester given that lightning strikes the phase conductor A.

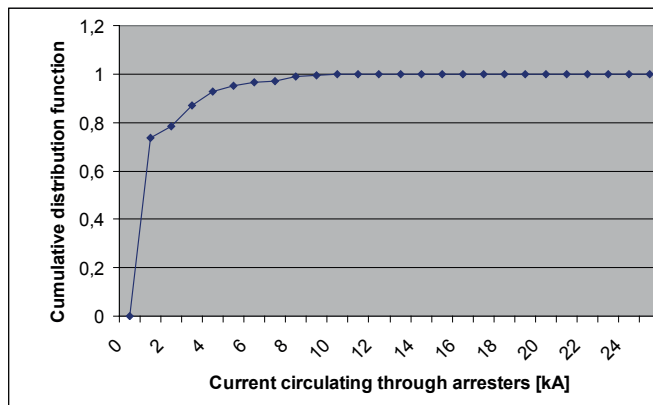


Figure 12: CDF of the current in arrester given that lightning strikes the adjacent tower.

Figure 13 shows the total CDF of the lightning current in the arrester. With EMTP-RV simulations it is determined that lightning strike currents in the range 0-200 kA, will cause currents circulating in the arrester in the range 0-25 kA. The median value (50 %) of the current circulating through the arrester is 2 kA. This total cumulative distribution function shows that the probability to have a current circulating in LSA higher than 10 kA is 1%.

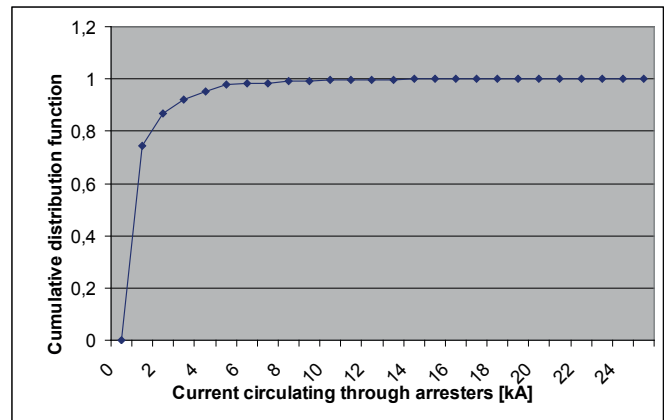


Figure 13: Total CDF of the lightning current through the arrester of the observed tower.

CONCLUSION

The determination of the cumulative distribution function of the lightning current circulating in LSAs is presented in this paper, and it can be applied for any transmission line, where LSAs are installed [17]. In order to simplify the problem, the following points of impact on the transmission line 110 kV Ston-Komolac were considered: the observed tower (no. 38 where the lightning real time measurement system is installed), both adjacent towers, the shield wire and the phase conductors of both adjacent towers. Through 4 successive steps, by using the software program EMTP-RV [18], and the configuration with data of the transmission line 110 kV Ston-Komolac (structure of towers, footing resistances, characteristics of LSAs installed on the line etc.) it was possible to estimate the cumulative distribution function of the lightning current circulating through a LSA which give us the probability for a lightning current circulating through LSA I_a , with a crest value higher than value i_0 .

This function can be useful for the selection and design of LSAs which will be installed on transmission lines to avoid outages due to lightning. Generally, the simulation results indicates, that the lightning strikes in the range 0-200 kA will cause currents through a LSAs in the range 0-25 kA, with the highest contribution from lightning striking the shield wire. It is important to note that these conclusions are done for a line with a shield wire. The application of the method on a line without shield wire would have led to other conclusions [16]. We should highlight also that a method similar to the one presented in this paper could be used to evaluate the energy constraints applied to LSAs.

ACKNOWLEDGMENT

This paper presents the results of research and simulations performed by the student G. Levačić during his internship in EDF R&D in Paris in 2009, under the supervision of Mr. A. Xémard. The research is associated with a pilot project of application of line surge arresters on the 110 kV overhead line Ston-Komolac in Croatia.

REFERENCE

- [1] M. Puharić, M. Mesić, M. Lovrić, J. Radovanović, S. Sadović, "Lightning Performance Improvement of 123 kV Line Ston-Komolac By Use Of Line Surge Arresters", CIGRE Symposium on Power System Management, Cavtat, 2008.
- [2] M. Mesić, J. Radovanović, D. Škarica, S. Sadović, "Improving of Reliability Overhead Line 110 kV Ston-Komolac by Line Surge Arrester Installation", Colloquium of Lightning and Power Systems, Kuala Lumpur, 2010.
- [3] A. Xémard, S. Sadović, T. Sadović, M. Mesić, A. Guerrier "Lightning current measurement on an overhead line equipped with line arresters", CIGRE, Paris, 2010.
- [4] CIGRE, "Lightning parameters for engineering applications", brochure 549, 2013.
- [5] CIGRE 63: "Guide to procedures for estimating the lightning performance of transmission lines", Working group 01 (lightning), 1991.
- [6] P. Pettersson, "A unified probabilistic theory of the incidence of direct and indirect lightning strikes", IEEE Transactions on Power Delivery Vol 6, N°3, 1991.
- [7] A. R. Hileman, "Insulation Coordination for Power Systems", book, 1999.
- [8] A. Sabot, "Coordination de l'isolement - Modèles électro-géométriques et fonctions de répartition des courants associés, livre électronique d'EDF, 1994.
- [9] R. Lambert, A. Xémard, G. Fleury, E. Tarasiewicz, A. Morched, "Probability Density Function of the Lightning Crest Current at Ground Level. Estimation of the Lightning Strike Incidence on Transmission Line", IPST, Budapest, 1999.
- [10] I. Uglešić, "Overvoltages in networks, High voltage techniques - Lectures", University of Zagreb
- [11] A. Xémard, S. Denetière, J. Michaud, P.Y. Valentin, Q. Bui-Van, A. Dutil, M. Giroux, J. Maheserdjian, "Methodology for the calculation of the lightning flashover rate of a line with or without line surge arresters", report CIGRE C4-101, 2006.
- [12] M. Puharić, M. Lovrić, J. Radovanović, Z. Čosić, S. Sadović, "Line Surge Arrester Application Pilot Project" 27th International Conference on Lightning Protection - ICLP, Avignon, 2004.
- [13] G. Levačić, "Application of line arresters on high voltage transmission line", graduate work, Paris, 2009.
- [14] H. W. Dommel, EMTP Theory Book, WP 5.1. Portland, Oregon, USA: Bonneville Power Administration
- [15] IEC TR 60071-4: "Insulation co-ordination Part 4: Computational guide to insulation co-ordination and modelling of electrical networks", 2003.
- [16] CIGRE, "Use of surge arresters for lightning protection of transmission lines", brochure, study committee C4, 2011.
- [17] CIGRE, "Evaluation of lightning shielding analysis methods for EHV and UHV DC and AC transmission lines", brochure 704, 2017.
- [18] EMTP-RV, www.emtp-software.com

Denisa Galzina

denisa.galzina@hops.hr

Croatian Transmission
System Operator Ltd.**Eraldo Banovac**

eraldo.banovac@zg.t-com.hr

Croatian Energy
Regulatory Agency**Tomislav Tomiša**

tomislav.tomisa@fer.hr

Faculty of Electrical
Engineering and Computing

Railway System Impact on Voltage Quality at the Level of the Croatian Transmission Network

SUMMARY

Railway systems are single-phase loads, connected to two-phase of the three-phase supply network. Therefore, they negatively affect the voltage quality, primarily the voltage unbalance. In addition to voltage unbalance, railway systems inject current harmonics into the network due to controllable diode or thyristor drives used to operate the train.

The paper gives a short theoretical description of the harmonic distortion and the voltage unbalance as well as the results of the voltage quality measurement. Moreover, the paper shows the impact of the railway system on the transmission network in the case that the facilities are connected to the 110 kV voltage level.

KEYWORDS

Railway system, voltage quality, voltage harmonics, voltage unbalance

INTRODUCTION

In the last decade, the Third energy package and the Clean energy for all Europeans package (so-called 'Winter Package') represent two major milestones in the frame of the EU energy legislation. The Clean energy for all Europeans package consists of eight legislative acts and represents a major step towards decarbonizing energy, facilitating better consumer outcomes and completing the Energy Union.

The Third energy package created a requirement for European network codes that cover grid connections, markets, and system operation. According to Hancher and Winters [1], »networks are often referred to as the 'hardware' of a well-functioning wholesale market«. In fact, operational security of transmission networks is crucial for the functioning of a sustainable electricity market. The network codes are designed to ensure a secure and competitive electricity market across Europe. A voltage deviation management procedure is prescribed in Article 19 of the Commission regulation (EU) 2017/2196 establishing a network code on electricity emergency and restoration [2] as follows: the procedure for the management of voltage deviations of the system defence plan shall contain a set of measures to manage voltage deviations outside the operational security limits set out in Article 25 of the Commission regulation (EU) 2017/1485 establishing a guideline on electricity transmission system operation [3]. Moreover, Article 17 of the Commission regulation (EU) 2017/2196 describes the

automatic scheme against voltage collapse of the system defence plan, which may include a scheme for low voltage demand disconnection, a blocking scheme for on load tap changer and system protection schemes for voltage management.

In general, poor voltage quality can cause high costs for both the transmission system operator and network users, and technical solutions are very expensive [4]. Railway systems, supplied by the high voltage network, represent the main source of voltage unbalance, leading to voltage quality problems that affect the normal operation of the equipment connected to the point of common coupling or in the rest of power network [5]. Furthermore, with the use of motor starters and variable speed drives (which represent non-linear loads), they inject harmonic currents directly into the supply network causing harmonic voltages throughout the network [6].

Locating the source of disturbance at supplier and customer's point of common connection is important criteria in power quality assessment. Voltage quality problems, such as harmonics and unbalance, have both technical and economic consequences. Power quality assessment and localization of disturbance sources are becoming matters of great interest to both utilities and customers [7].

Nowadays, great attention is paid to the problem of power quality. This can be explained by the following arguments. Firstly, there is a trend towards an increase in technologically advanced equipment and production

processes. This imposes high requirements on the quality of power to be supplied. In this context, it should be stressed that electricity has a market-driven value. Furthermore, most of the modern loads are nonlinear and their number is increasing. The nonlinear load generates harmonics, which leads to the distortion of voltage and current wave forms and changes in the characteristics of supplied power. This requires an increase in the power of the system by the value spent on their distortions [8].

The content of the harmonics level in the supply voltage has a significant effect on the efficiency of electricity usage. Therefore, there is a need for using a voltage quality monitoring system to ensure continuous monitoring of the harmonics level throughout the power system. Voltage quality monitoring system allows a real time determination of the harmonics direction and levels in the supply voltage.

The effect of non-sinusoidal power supply can be approximately mitigated by device derating, by installing K-rated distribution transformers and harmonic filters, or by complex network management, which aggregate the non-linear consumers [9].

Altogether, railway systems represent an undesirable load on the supply network.

DISTURBANCES

A number of studies point to railway influence on power supply system. Bearing in mind the findings in [5-6] and [10-11], it is important to clarify that voltage harmonics and voltage unbalance are disturbances of main interest.

2.1. Voltage Harmonics-

Harmonics are mathematical descriptions of current or voltage waveforms. Ideally, voltage and current waveforms are perfect sinusoids. However, because of the increased presence of electronic and other non-linear loads, these waveforms often become distorted. This deviation from a perfect sine wave can be represented by harmonics-sinusoidal components with a frequency that is an integral multiple of the fundamental frequency [12]. Thus, a pure voltage or current sine wave has no distortion and no harmonics, and a non-sinusoidal wave has distortion and harmonics, as shown in Figure 1.

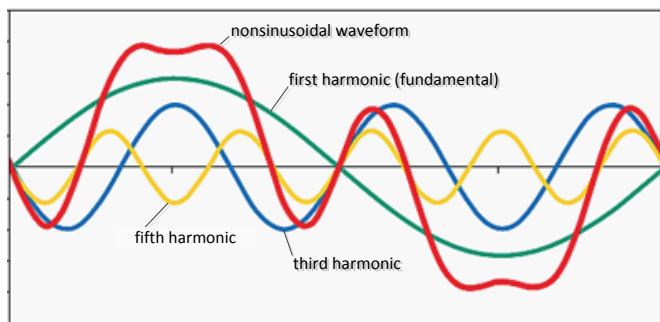


Figure 1. Distorted waveform consisting of the fundamental, third and fifth harmonics

Harmonic disturbances are generated generally from equipment with a non-linear voltage-current characteristic. A variety of harmonic sources exists – magnetic core equipment (like transformers, electric motors, generators, etc.), arc furnaces, arc welders same as electronic and power electronic equipment [10].

The total harmonic distortion (THD) is used to quantify distortion. THD expresses the distortion as a percentage of the fundamental (pure sine) of voltage and current waveforms. It is defined as:

$$THD_V = \frac{\sqrt{\sum_{h=2}^{40} V_h^2}}{V_1} \quad (1)$$

where: THD_V – total harmonic distortion, V_h – effective value of the h^{th} harmonic, h – harmonic order, V_1 – fundamental harmonic.

Voltage distortion affects not only sensitive electronic loads, but also electric motors and capacitor banks. In electric motors, negative sequence harmonics (the sequence of which is opposite to the fundamental sequence, i.e. 5^{th} , 11^{th} , 17^{th}) produce rotating magnetic fields. These fields rotate in the opposite direction of the fundamental magnetic field and could cause overheating and mechanical oscillations in the motor-load system.

Many problems are also caused by 3^{rd} harmonic and odd multiples of the 3^{rd} (9^{th} , 15^{th} , 21^{st} , etc.). These harmonics are called “triplens” (the A-phase triplen harmonics, B-phase triplen harmonics and C-phase triplen harmonics are all in phase with each other). According to [13], they will add rather than cancel on the neutral conductor of a 3-phase, 4-wire system (this can overload the neutral conductor if it is not sized to handle this type of load).

Harmonic problems are mitigated by linear chokes, multi-pulse convertor systems, passive or active filters, and broadband or tuned filters [14].

2.2. Voltage Unbalance

The three-phase power system is called balanced or symmetrical if the three-phase voltages and currents have the same amplitude and are phase shifted by 120° with respect to each other. If these conditions are not met, the system is called unbalanced or asymmetrical [15].

Voltage unbalance used to be defined as the maximum deviation from the average of the three-phase voltages, divided by the average of the three-phase voltages, expressed in percent [16].

$$V_{UN}[\%] = \frac{\max \text{voltage deviation from avg line voltage}}{\text{avg line voltage}} \cdot 100 \quad (2)$$

The unbalance is more rigorously defined using symmetrical components. The ratio of the negative-sequence component to the positive-sequence component can be used to specify the percent unbalance [12].

$$V_{UN}[\%] = \frac{\text{negative sequence voltage component}}{\text{positive sequence voltage component}} \cdot 100 \quad (3)$$

The positive and negative sequence voltage components are obtained by resolving three-phase unbalanced line voltages V_{ab} , V_{bc} , and V_{ca} into two symmetrical components – V_p and V_n . The two balanced components are given by:

$$V_p = \frac{V_{ab} + a \cdot V_{bc} + a^2 \cdot V_{ca}}{3} \quad (4)$$

$$V_n = \frac{V_{ab} + a^2 \cdot V_{bc} + a \cdot V_{ca}}{3} \quad (5)$$

where: $a = 1 \angle 120^\circ$, and $a^2 = 1 \angle 240^\circ$.

Unbalance is a serious power quality problem [17]. The unbalance affects the voltage quality, but also the additional heating of the generator rotor due to the inverse magnetic field caused by the inverse currents. The unbalance, therefore, affects the safety, reliability and economy of the transmission system. It is also important to mention that unbalance can cause great material damage as well as damage due to the inability of the electricity supply.

VOLTAGE QUALITY MONITORING

It is important to ensure voltage quality due to the susceptibility of industrial installations and end-user equipment to voltage disturbances. Therefore, voltage quality monitoring systems are implemented worldwide with the differences between countries in the choice of monitored voltage quality parameters. Regarding the voltage quality parameters monitored in different European countries, it is important to mention that a total of 15 countries are monitoring voltage unbalance [18].

The reason to monitor voltage quality parameters directly relied to railway system operation is spreading of electrified railway network and increase in traffic density and velocity, which causes higher power demand and,

At the transmission network level, CP95 value of voltage harmonic distortion is 1.15%, as is shown in Figure 7.

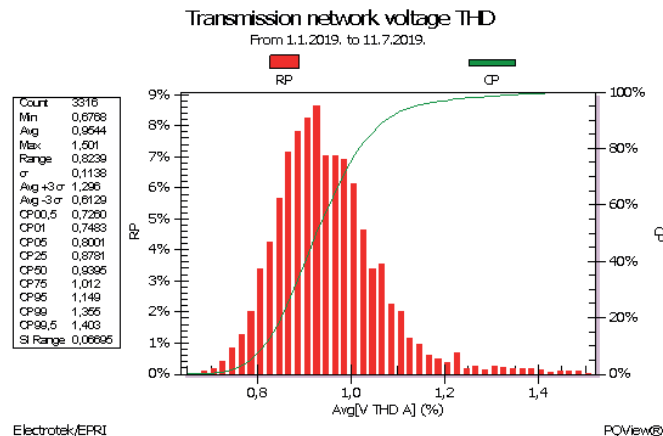


Figure 7. CP95 histogram for voltage THD in the transmission network

4.2. Voltage Unbalance Measurements

Figures 8-11 show the measured voltage unbalance values in the facilities containing a railway system transformer field. Voltage unbalance measurements were performed on the voltage bus where the railway transformers are connected, expecting the maximum value of the voltage unbalance.

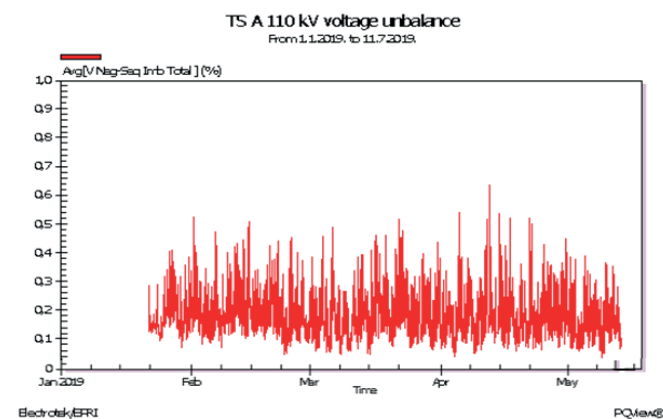


Figure 8. Value of the voltage unbalance in the facility A (TS 110 kV)

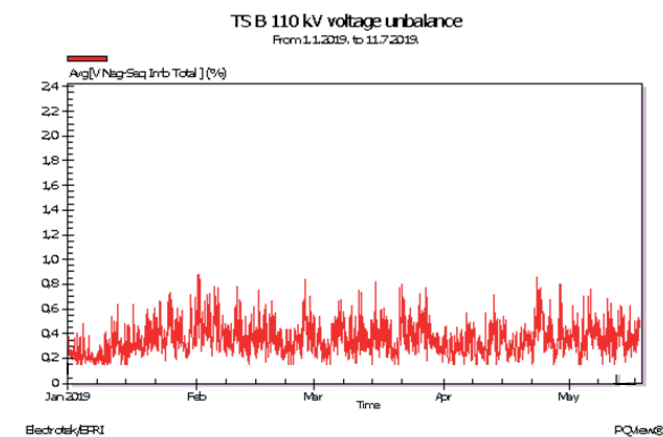


Figure 9. Value of the voltage unbalance in the facility B (TS 110 kV)

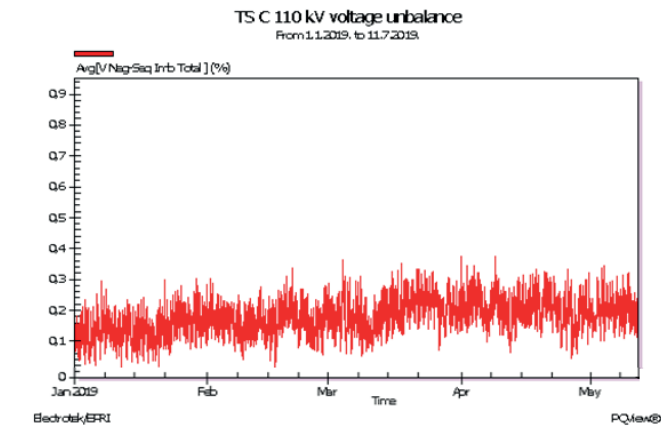


Figure 10. Value of the voltage unbalance in the facility C (TS 110 kV)

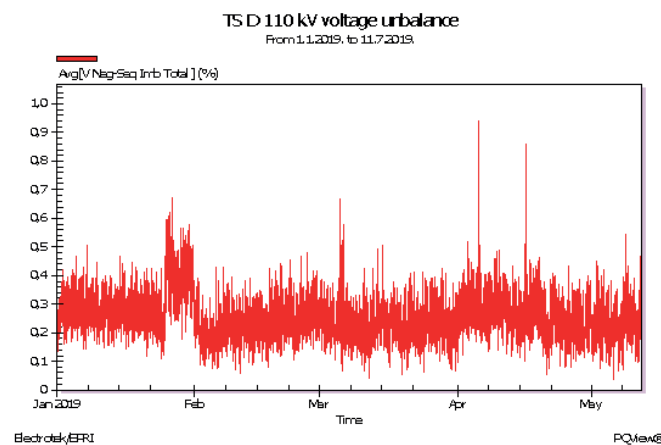


Figure 11. Value of the voltage unbalance in the facility D (TS 110 kV)

The voltage unbalance value measured in facility A is less than 0.65%, and in facility B does not exceed 0.9%. A slightly lower unbalanced load with voltage unbalance about 0.35% is measured in facility C, while voltage unbalance measured in facility D is about 0.95%.

The highest values of unbalance appear on the common busbars of the railway facility. Taking into consideration the measured voltage unbalance values shown in Figures 8-11, it can be concluded that the 110 kV transmission network is robust enough to overcome the negative influence of the railway system facilities regarding the voltage unbalance.

Overall at the level of the Croatian transmission system as a whole, the unbalance is less than 0.35% (Figure 12).

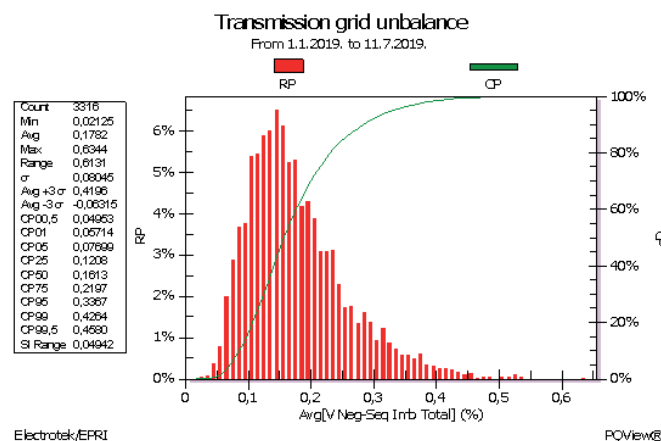


Figure 12. CP95 histogram for voltage unbalance in the transmission network

CONCLUSION

The railway system is one of the largest voltage quality »polluters« since it is a specific load supplied from two-phase of the three-phase network causing a voltage unbalance. Due to the operation of the thyristor converters in the trains, it also causes a large voltage distortion.

Therefore, it is necessary to verify the impact of the railway system operation on the transmission network, as it may interfere with the operation of other customers connected to the network. In addition, railways are of great socio-economic importance, and their negative impact on the transmission system cannot be eliminated by disconnecting them from the network.

Although the railway is theoretically a major problem for any supply grid, the results of this study show that it does not cause any major issues on the 110 kV voltage level of the Croatian transmission network. In fact, the total consumption of the railway system is relatively small, due to occa-

sional energy needs (train passage). Thus, the average monthly demand in some railway substations is equal to 20% of the installed power. This is the reason why it does not significantly reduce the voltage quality of the transmission network. Taking into consideration the measured voltage unbalance values, it can be concluded that the 110 kV transmission network is robust enough to overcome the negative influence of the railway system facilities regarding the voltage unbalance.

In conclusion, high values of voltage unbalance at the level of the Croatian transmission network may occur only in the case of a single phase drop-out (conductor break due to ice or mechanical damage), rather than a connection of the railway facility to the grid.

Since there is no infrastructure for the high-speed railway in Croatia at this time, taking into account the experience of other European countries, it is certain that there will be no augmentation of the overall railway impact on power quality in the near future.

REFERENCE

- [1] L. Hancher, B. M. Winters, "The EU Winter Package, Briefing Paper", Allen & Overy LLP, Amsterdam, The Netherlands, February 2017
- [2] COMMISSION REGULATION (EU) 2017/2196 of 24 November 2017 establishing a network code on electricity emergency and restoration, Official Journal of the European Union, L 312/54, 28.11.2017
- [3] COMMISSION REGULATION (EU) 2017/1485 of 2 August 2017 establishing a guideline on electricity transmission system operation, Official Journal of the European Union, L 220/1, 25.8.2017
- [4] D. Galzina, "Evaluation of voltage quality indicators in power transmission network", Doctoral thesis, Faculty of electrical engineering and computing, University of Zagreb, 2019, p. 89
- [5] F. Peticaroli, "Electrical systems for transportation", Milan, CEA, 2001
- [6] A. Baggini, "Handbook of power quality", Wiley & Sons, 2008
- [7] M. Hasanuzzaman Shawon, S. Barczentewicz, J. Kowalski, "Identification of asymmetry in power system: Different case studies", IEEE Electric Power Quality and Supply Reliability Conference, Tallin, Estonia, 29-31 August 2016
- [8] K. Suslov, N. Solonina, D. Gerasimov, "Assessment of an impact of power supply participants on power quality", 18th International Conference on Harmonics and Quality of Power (ICHQP), September 2018
- [9] M. A. Taher, S. Kamel, Z. M. Ali, "K-Factor and transformer losses calculations under harmonics", Proc. 2016 IEEE Eighteenth International Middle East Power Systems Conference (MEPCON), Cairo, 27-29 December 2016, pp. 753-758
- [10] A. Dan, P. Kiss, "Effect on Power Quality of the High Power Electric Traction", Budapest University of Technology and Economy, April 2006
- [11] R. S. Thorat, M. M. Deshpande, "Power quality issues in railway electrification", International Journal of Computer Science and Engineering, 2016, Vol. 4, Issue 1, pp. 37-39
- [12] Pacific gas and electric company, "Power System Harmonics", January 1993
- [13] A. Gado, "Effect of single-phase, non-linear loads, as sources of harmonic currents in low voltage electrical distribution system", CIRED 21st International Conference on Electricity Distribution, Frankfurt, 6-9 June 2011, Paper 0061, p. 1/4
- [14] G. Sandoval, J. Houdek, "A review of harmonic mitigation techniques", APQ Power, 2005
- [15] UIE Guide to quality of electrical supply for industrial installations, Part 1: General introduction to electromagnetic compatibility (EMC), types of disturbances and relevant standards, 1994
- [16] P. Pillay, M. Manyage, "Definitions of Voltage Unbalance", IEEE Power Engineering Review, May 2001, pp. 50-51
- [17] J. Driesen, T. Van Craenenbroeck, "Voltage disturbances, Introduction to unbalance", European Copper Institute, Katholieke Universiteit Leuven and Copper Development Association, 2002
- [18] Council of European Energy Regulators (CEER), "6th CEER Benchmarking Report on the Quality of Electricity and Gas Supply", 2016
- [19] D. Serrano-Jiménez, L. Abrahamsson, S. Castaño-Solis, J. Sanz-Feito, "Electrical railway power supply systems: current situation and future trends", International Journal of Electrical Power & Energy Systems, Vol. 92, November 2017, pp. 181-192
- [20] A. Tabakhpour, A. Mariscotti, M. A. Abolhassani, "Power quality conditioning in Railway electrification: A comparative study", IEEE Transactions on Vehicular Technology, Vol. 66, Issue 8, Aug. 2017
- [21] A. Mariscotti, "Measuring the power quality of railway networks", IEEE Instrumentation and Measurement Technology Conference, pp. 686-690, June 2010
- [22] A. Mariscotti, "Measuring and analyzing power quality in electric traction systems", International Journal of Measurement Technologies and Instrumentation Engineering, pp. 21-42, December 2012
- [23] A. Mariscotti, "Results on the power quality of French and Italian 2x25 kV 50 Hz railways", IEEE International Instrumentation and Measurement Technology Conference Proceedings, pp. 1400-1405, Graz, 2012
- [24] José Conrado Martínez Acevedo, Antonio Berrios Villalba, Eugenio Peregrin García, "Current situation and prospect of electric traction systems used in High-Speed railways", 360. revista de alta velocidad, nr. 5, pp. 49-69, June 2018
- [25] Narodne novine, br. 67/17, "Mrežna pravila prijenosnog sustava", 2017.

Mičo Klepo

mklepo@hera.hr

Croatian Energy Regulatory Agency,
Ul. grada Vukovara 14.
10 000 Zagreb**Vladimir Mikuličić**

vladimir.mikulicic@fer.hr

Faculty of Electrical Engineering and Computer Science,
Unska 3.
10 000 Zagreb**Zdenko Šimić**

zdenko.simic@gmail.com

Faculty of Electrical Engineering,
Computer Science and Information Technology Osijek,
Kneza Trpimira 2B.
31000 Osijek

Peak Plant Models in the Electric Power System Model of Reliability and Availability

SUMMARY

The work sets out the results of the theory/methodological refinement of models whereby peak generating plants are included in the reliability and availability patterns of electricity systems while operational planning operations are taking place. Account shall be taken of the technical and energy characteristics of such generating units, as well as of the specific conditions and requirements imposed on such generating units, resulting from their location and the role in covering peak loads and consumption of the electricity system.

KEYWORDS

Peak plant model, plant failure during operation, plant failure during start-up, postponable outage, power system availability and reliability

INTRODUCTION

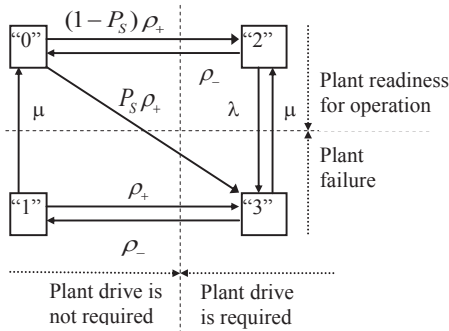
The general problem of data collection, statistical treatment and calculation of parameters and indicators for the establishment of generating units models during operational planning operations, as well as the means of access and solutions to the problem of the incorporation of generating units in the reliability and availability model of the electricity system, have so far been further processed and exposed in a number of works (L1 to L16). Processing in this work includes a general model of a peak load power plant, but also complex models, an extended model which distinguishes between peak plants and start-up failures at the start and during operation, and the model of the peak load plant with the possible postponement of exit from the operation.

The complex models shall be with a view to distinguishing between failures during start-up and failures during operation mode of the peak load plant, but also to include the possibility of plant outage postponability, depending on the gravity and type of failure during operation. This introduces the possibility to include additional demands and operative characteristics in the calculations of indicators of the availability and reliability of generating units which cover peak portions of the load diagram, which means that they are relatively often entering and leaving the plant, often changing rapidly the load level, which is subject to specific additional stress and heavier operating conditions, including special additional requirements and operational features. Of course, the possibility of distinguishing the degree and the seriousness of failure at the starting and running of the peak generating

unit opens the possibility for part of the faults incurred at the start to be removed during the presence of the need or by the requirement to drive the peak generating unit, and to enter the plant. In a similar manner, the distinction between the degree and the seriousness of failure during operation, or rather, by introducing the possibility that depending on the degree of failure, the peak plant remains in operation, allows for the extension of its operation. Both have a direct impact on the status and indicators of the availability and reliability of the power system.

FOUR-STATE PEAK PLANT MODEL

The four-state peak plant model, as shown in Figure 1, shall be used to include in the estimation of the reliability and availability indicator of the electric power system the plants that cover the peak part of the load diagram, which are subjected to higher stresses due to frequent entries and exits from operation i.e. start-ups and shut-offs [L9], [L10] and [L11]. In addition to the faults occurring during the operation, failures can occur when the plant is placed in operation. The failure of the installation shall result in the plant being unable to meet the prescribed load for part of for the entire duration of the need for that load. The repeated reattempt at commissioning of the same plant for a specified period of service shall not be treated as more than one starting failure. Therefore, the probability of the commissioning plant shall be carefully assessed in case when data are kept for the overall number of putting into service only.



Legend (Figure 1):

- “0” - the state of the plant reserve shut-down,
- “1” - the state of the plant failure when drive is not being required,
- “2” - the state of the plant drive when drive is being required,
- “3” - the state of the plant failure when drive is being required,
- λ - the plant failure rate,
- μ - the plant repair rate,
- ρ_+ - the rate of occurrence of the need for the drive,
- ρ_- - the rate of termination of the need for the drive,
- P_s - the probability of plant failure during the start-up.

Figure 1 – The four-state model of the peak load plant

There is no transition from the status of the plant reserve shut-down to the condition of failure when its activation is not required, due to the fact that the number of such transition is negligible and it is reasonable to assume that the plan cannot fail when it is shut off because of the reserve or if it is not in operation. Any discovery of conditions that may lead to forced unavailability on the basis of a back-up disconnection may be associated with cases of repeated failures, such as the occurrence of such conditions during inspection or overhaul.

According to Figure 1, the Markov process, which describes the four-state model of the peak load plant, describes the following system of linear differential equations:

$$\begin{aligned} \dot{P}_0(t) &= -\rho_+ P_0(t) + \mu P_1(t) + \rho_- P_2(t) \\ \dot{P}_1(t) &= -(\mu + \rho_+) P_1(t) + \rho_- P_3(t) \\ \dot{P}_2(t) &= (1 - P_s) \rho_+ P_0(t) - (\rho_- + \lambda) P_2(t) + \mu P_3(t) \\ \dot{P}_3(t) &= P_s \rho_+ P_0(t) + \rho_+ P_1(t) + \lambda P_2(t) - (\rho_- + \mu) P_3(t) \end{aligned} \quad (1)$$

where:

$\dot{P}_i(t) = \left(\frac{dP_i(t)}{dt} \right)$ - is the derivation of probability of state “i” in relation to time “t”,

$P_i(t)$ - is probability of state “i” (i = 0, 1, 2, ..., n).

Under the assumption that when t = 0, the power plant is functional, the starting conditions are:

$$P_0(0) = 1, P_1(0) = 0, P_2(0) = 0, P_3(0) = 0. \quad (2)$$

A stationary solution is being sought, i.e. the solution when is

$$\dot{P}_n(t) = 0; n = 0, 1, 2, 3. \quad (3)$$

Under condition (3), system (1) takes on a new form:

$$\begin{aligned} 0 &= -\rho_+ P_0 + \mu P_1 + \rho_- P_2 \\ 0 &= -(\mu + \rho_+) P_1 + \rho_- P_3 \\ 0 &= (1 - P_s) \rho_+ P_0 - (\rho_- + \lambda) P_2 + \mu P_3 \\ 0 &= P_s \rho_+ P_0 + \rho_+ P_1 + \lambda P_2 - (\rho_- + \mu) P_3 \end{aligned} \quad (4)$$

System (4) with an identity equation

$$P_0 + P_1 + P_2 + P_3 = 1 \quad (5)$$

results in the stationary probability of states :

$$\begin{aligned} P_0 &= \frac{\mu}{\rho_+} (\mu + \rho_+ + \lambda + \rho_-) / \Delta \\ P_1 &= (\lambda + P_s \rho_+) / \Delta \\ P_2 &= \mu \left[\frac{1}{\rho_+} (\mu + \rho_+) + 1 - P_s \right] / \Delta \\ P_3 &= \frac{1}{\rho_-} (\mu + \rho_+) (\lambda + P_s \rho_+) / \Delta \\ \Delta &= \frac{\mu}{\rho_+} (\mu + \rho_+ + \lambda + \rho_-) + (\lambda + P_s \rho_+) \left[1 + \frac{1}{\rho_+} (\mu + \rho_+) \right] + \mu \left[\frac{1}{\rho_+} (\mu + \rho_+) + 1 - P_s \right] \end{aligned} \quad (6)$$

In order to determine model parameters, the following data is needed:

g - the average time that the plant spent in operation, between the forced outage states due to failures, excluding forced outages as a result of faults or defects during start-up,

m - the average of the repair period or the average duration of the failure in the event of the failure,

Y - the average time that the plant is in operation on presence of the need for drive and the load, i.e. the duration of the work cycle,

X - the average duration of spare shutdown between the time periods when work is required, excluding maintenance time and other times of planned unavailability of the plant, where the following criterion is valid:

$$X + Y = \frac{RH}{g}, \quad (7)$$

u - the number of the plant failures,

Ω - the number of times when the plant is shut down for economic reasons,

\mathcal{G} - the total number of the plant launches, i.e. entries into service,

P_1 - the probability of the plant failure during the entry into service, in terms of the expression:

$$P_s = \frac{NPS}{NUP + NPS},$$

NPS - the number of the plant failures during the entry into service,

NUP - the number of the successful entries.

The Ω model parameters are:

$$= \frac{u - P_s * \mathcal{G}}{SP} = \frac{1}{g}; \mu = \frac{u}{SK} = \frac{1}{m}; \rho_+ = \frac{g}{RH - \frac{g}{\rho_+}} = \frac{1}{X}; \rho_- = \frac{(1 - P_s) * \mathcal{G}}{SP} = \frac{1}{Y} \quad (8)$$

where:

SP - the number of hours of operation of the peak plant,

RH - the number of hours of the peak plant availability for work,

SK - the number of hours of the peak plant inability for work.

The risk of the plant failure may be defined as

$$FOR = \frac{P_1 + P_3}{P_1 + P_2 + P_3} \quad (9)$$

However, this is not a good measure of risk that the plant will not be able to cover the intended part of the peak load, provided it occurs. This measure is defined by the term

$$FOR_p = \frac{P_3}{P_2 + P_3} = \frac{(P_3 + \frac{\lambda}{\rho_-})(\mu + \rho_+)}{\mu[\frac{1}{\rho_-}(\mu + \rho_+) + 1] + \frac{\lambda}{\rho_-}(\mu + \rho_+)} \quad (10)$$

In fact, it is a reasonable conditional probability in relation to the phenomenon and the length of the need for drive, which means provided that the need arises. As the duration of operation is prolonged, thus P_1 tends to zero, and the risks of the plants in terms of (9) and (10) are put on an equal footing. A conditional probability can easily be estimated as follows: for a longer period of time, an estimated value of P_2 can be obtained as a ratio between the hours of operation (SP) and the sum of the hours of availability (RH) and the contingency hours (SK) (L11 and L13):

$$\hat{P}_2 = \frac{SP}{RH + SK} \quad (11)$$

where:

P_2 - the estimated value of the peak plant probability of operation when operation is needed.

Thus, the period of time of situation when the plant is out of operation due to repairs, maintenance, or any other planned shutdown is excluded. The probability of failure, i.e. $P_1 + P_3$, is estimated as the ratio of the number of hours when the plant is not available for work due to failures (SK) and the sum of the number of hours when it is available (RH) and the contingency hours (SK):

$$(\hat{P}_1 + \hat{P}_3) = \frac{SK}{RH + SK} \quad (12)$$

where:

P_1 - the estimated value of the peak plant failure probability when drive is not needed,

P_3 - the estimated value of the peak unit failure probability when drive is needed.

In order to determine the risk of unavailability of the plant in the event of the need for drive, taking account of the estimated values by terms (11) and (12), factor ξ shall be introduced into term (10) determined as

$$\xi = \frac{P_3}{P_1 + P_3} = \frac{\mu + \rho_+}{\mu + \rho_+ + \rho_-} = \frac{\frac{1}{m} + \frac{1}{X}}{\frac{1}{m} + \frac{1}{X} + \frac{1}{Y}} \quad (13)$$

after which the probability of the plant unavailability for operation when drive is needed, i.e. the estimated value of this probability, shall have the following forms:

$$FOR_p = \frac{P_3}{P_2 + P_3} = \frac{\xi(P_1 + P_3)}{P_2 + \xi(P_1 + P_3)} \quad (14)$$

$$\hat{FOR}_p = \frac{\xi(\frac{SK}{RH + SK})}{\frac{SP}{RH + SK} + \xi(\frac{SK}{RH + SK})} = \frac{\xi^*(SK)}{SP + \xi^*(SK)} \quad (15)$$

The ξ factor ξ for weighting is the contingency hours (SK) reflecting the cumulative number of contingencies occurring during the period of operation. Depending on the operating cycle and the duration of contingencies, this factor represents the contribution of hours of the plant failure when operation needed to the total number of hours when the plant is disabled for operation. Thus, this factor includes in the equation the effect of the operation cycle and the duration of the peak plant failures, reducing the number of hours of failure by the above-mentioned effects.

There is a clear similarity between the factor ξ defined by the term (13) with the correction or adjustment factor modifying the base plant model in order to cater for the calculation of the reliability and availability parameters

of the plant design, i.e. its failure can only start during the load time of the plant and not over the plant reserve shut-down time between the periods of need for operation (L13). The difference between them is that the modified base plant model does not include a presumption that any forced failure can arise from the start or during the need for operation of the plant, which leads to an understatement of the amount of that factor.

The correction error is low if the plant repair time is relatively long compared to the plant average suspension time for the reserve ($m \gg X$). Where the repair time is short, factor ξ is approaching the unit. The corrected number of contingency hours during the period of need for operation may be estimated as follows:

$$SK_{cor} = \xi \cdot (SK) \quad (16)$$

The following problem presents the difficulty of assessing the impact of a change in the duty cycle on the risk of unavailability of the plant when its operation is needed. Indeed, the risks of unavailability of the plant are in fact chosen at random in one way if they are working on a weekly basis, compared to the cycle of service with daily start and shut-down. It is possible to solve the problem in two ways.

The first is that records and data the outages of the plant exposed to operational cycles corresponding to the expected type of use, and on the basis of them, determine the model's parameters for the plant. Another way is to adapt the available statistical data to the plant's new mode and the calculation of model parameters for these new conditions. The adjustment should in particular relate to intermediate to the failure, the probability of failure at the start-up and the mean repair time of the plant. By extrapolation, account should be taken of the changes in the relative difficulties of the start and the load, the speed of the load changes and the urgency of the exits.

With the increasing number of plant covering the peak part of the system load the need to determine as precisely as possible the parameters for the availability budget of each of these plants is also growing. Since in the first years of operation, i.e. in the case of new on-site plants, there is, as a general rule, insufficient 'good' data to determine the model parameters, it is then reasonable to apply the increased fault rates from the facility, i.e. the increased rate of failures.

The exposed fur-state model in addition to the peak facility may also be used for the layout and analysis of intermittent work, that is, the base drive firing a longer perimeter of work and spare exclusion, significantly different from the operating cycle and the duration of the work at the peak operation. The distinction between intermittent work and working with a base charge is not always clear. The limits shall only determine the duration of the operation. In fact, according to the term (13), the value of the weight factor ξ is higher and tends to unit as the duration of the need for the operation of the plant is in excess of the periods of spare exclusion and repair. In this case, the conditional probability determined by the phrase (10) is to aim for the ratio $m/(m + g)$, which is the analytical equivalent of the contingency risk (FOR), subject to a long load condition. Thus, the conditional probability of the plant unavailability, provided that the need arises, becomes the same as the risk of the plant failure as the factor ξ is approaching the unit.

In the four-state model, the frequency of the plant failure shall determine the product of the probability of unit failure when operation is needed (state "3"), i.e. P_3 , and the sum of the plant repair rate and the rate $\xi\xi$ of the need for the drive termination.

$$f_3 = P_3(\mu + \rho_-) \quad (17)$$

This value corresponds to the product of the probability of the plant unavailability when its operation is needed as defined by the term (14), the probability of the occurrence of the need for the operation ($P_2 + P_3$) and the rate of the plant shut-downs, whether due to the repair or the operation is no longer needed.

The frequency of occurrence of the operating state when operation is needed, i.e. state "2" in the peak load model, shall be equal to the product of the probability of this state and to the sum of the rate of the need for the drive termination and the plant failure rate:

$$f_2 = P_2(\rho_- + \lambda) \quad (18)$$

It is the sum of the frequency of transition from the state "2" to "0" and "3." For a longer time period, the ratio between the two frequencies is equal to

the g/Y ratio, i.e. the number of transitions from the state “2” to the state “0” and from the state “2” to the state “3.”

Where more detailed data are known about the number of transitions between states, i.e. the residence times under the individual the states, then the modelling parameters may also be determined as follows.

The average duration of the state “2” is determined by the term

$$T_2 = \frac{l}{\rho_+ + \lambda} = \frac{gX}{g + X} = \frac{\Sigma T_2}{N_{2,0} + N_{2,3}} \quad (19)$$

where:

ΣT_2 - the cumulative retention in the state “2”, i.e. (SP),

$N_{2,0}, N_{2,3}$ - the number of transitions from the state “2” to the state “0” and “3” respectively, for which:

$$N_{2,0} = \frac{\Sigma T_2}{Y} \quad (20)$$

$$N_{2,3} = \frac{\Sigma T_2}{m} \quad (21)$$

With that terms, based on data regarding operation statistics, the parameters of g and Y shall be determined.

The transitions from the state “0” are possible only to the states “2” and “3”. The time period spent in the state “0” is determined as follows:

$$T_0 = \frac{1}{\rho_+} = X = \frac{\Sigma T_0}{N_{0,2} + N_{0,3}} \quad (22)$$

where:

ΣT_0 - the cumulative duration of the state “0”, i.e. (RH-SP),

$N_{0,2}, N_{0,3}$ - the number of transitions from the state “0” to state “2” and “3” respectively, for which:

$$N_{0,2} = \frac{(1 - P_s)\Sigma T_0}{X} \quad (23)$$

$$N_{0,3} = \frac{P_s \Sigma T_0}{X} \quad (24)$$

With that terms, based on data regarding operation statistics, the parameters P_3 and X shall be determined. The parameter m still remains. It is possible to determine it as follows. The plant failure frequency, whether or not its operation is needed (states “1” and “3”), is equal to the product of the sum of the probabilities of the states “1” and “3” and the transition rates from these states:

$$f_{1,3} = \mu P_1 + \mu P_3 = \mu(P_1 + P_3) \quad (25)$$

Whereas the average duration of the failure to operate or to repair, notwithstanding the need for operation, is equivalent to an inverse of the repair frequency value, the following shall be valid:

$$m = \frac{1}{\mu} = \frac{P_1 + P_3}{f_{1,3}} = \frac{\Sigma(T_1 + T_3)}{N_1 + N_3} \quad (26)$$

where:

$\Sigma(T_1+T_3)$ - the cumulative time of failure, i.e. (SK),

$(N_1 + N_3)$ - the total number of failures, i.e. the transitions to the states “1” and “3”.

A specific problem introduces the partial failure of the peak load plant. In that case, three approaches may be followed. The first is that partial failures should be set aside, which can be done if those failures do not contribute significantly to the number and duration of the faults in the power system, that is to say, depending on the other installations of the power system. The second is when these failures have a major impact on the operation of the power system, when more complex models are needed, which is the subject of special treatment in the following chapters. Finally, in the third approach, the baseline of the four-state model is retained as a basis for the calculation of the indicator, but the failure risk is used in the modified form.

Under partial contingency, it shall be assumed that the plant is loaded with a part load during the entire contingency period and the contingency hours shall be added to the full contingencies in the phrase (15), as the equivalent hours, resulting in an equivalent contingency risk of the facility;

$$F\hat{O}R_p = \frac{\xi^*(SK) + ekv(SK)}{SP + \xi^*(SK)} \quad (27)$$

where:

$ekv(SK)$ - the hourly equivalent of the plant partial failure obtained as follows:

$$ekv(SK) = \frac{\sum_{i=1}^{\pi} (O_i^{isp} * SK_i^{isp})}{O_{max}} ; \quad (28)$$

i - the ordinal number of the partial load outage ($i=1, 2, \dots, \pi$),

O_i^{isp} - the part of the load outage during outage »i«,

O_{max} - the maximum load of the plant in the observed period,

SK_i^{isp} - the duration of partial contingency »i«.

As regards the exposed four-state peak load model (Figure 1), i.e. the main model of the peak load, it is also necessary to add the following. In the most general case, this model may also be used for inclusion in the calculation of the reliability and availability indicators of the wind farm production unit. In order to be able to use the model as the wind farm model, it is necessary to label the state “plant drive is not required” as the state “not sufficient wind to drive plant”, while the state “plant drive is required” to label as the state “sufficient wind to drive plant”. Adequate, the state “0” of the plant spare shut-down status and the state “1” of the condition of the plant failure when the plant is not required to drive, shall become the condition of the suspension or the condition of the failure condition in the weather conditions when there is no sufficient wind for the plant to drive. On the other hand, the state “2” of the plant when the plant is required to drive and the state “3” of the plant failure when the plant is being sought, become the operational status or the condition of the plant failure in the weather conditions when the wind is sufficient to propel the wind farm. The duration of the weather conditions where there is no sufficient wind for the wind farm to drive shall also include the duration of the very strong wind or storm weather during which the wind farm must be removed from the operation for protection purposes. Finally, in order to be able to use the model as a wind farm model the rate of occurrence of the need for drive ρ_+ should be replaced by the rate of occurrence of weather conditions when wind is sufficient to propel (e.g. code ‘v’ – the rate of occurrence of sufficient wind time for the plant operation), while the rate of termination of the need for drive ρ_- should be replaced by the rate of weather conditions when the wind is not sufficient or is too high to propel the wind farm, i.e. the wind farm is switched off due to a thunderstorm.

Examples are provided below of the application of the four-state peak load model to two peak plants, namely: the peak load plant A, whose work cycles are short, often entrances and exits from the operation, thus covering the highest parts of the load diagram of the power system (daily work cycle), and peak load plant B, whose work cycles last longer, thus covering the intermediate parts of the load diagram of the power system (weekly working cycle).

Tables 1.1 and 1.2 present for peak load plant A and peak load plant B the input data to calculate the input parameters and the model parameters of the peak generating units, the stationary state probabilities for the input parameters thus determined, and the other parameters and indicators as the results of the four-state model application, relevant for the reliability and availability patterns of the power systems while operational planning operations are taking place.

Table 1.1 - The four-state peak load plant model parameters, the stationary probabilities of states and the other indicators of the peak load plant A

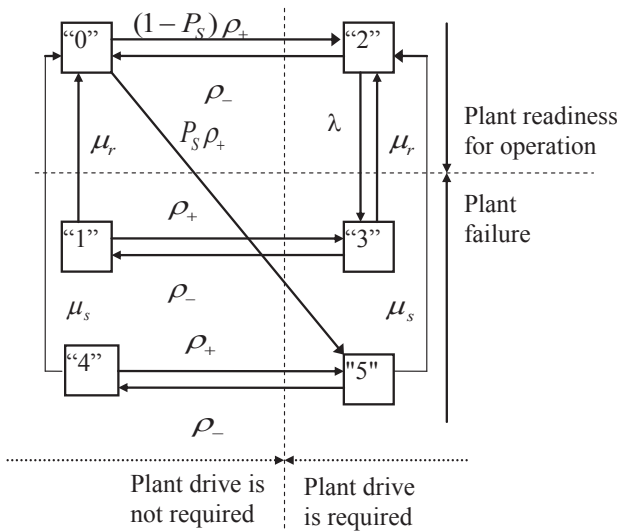
Data for the calculation of the plant parameters and the parameters of the peak load model states		Stationary state probabilities of the peak load plant		Other parameters and model indicators of the peak load plant operational conditions	
g	714,3	P_0	0,27020	P_1+P_3	0,09216
m	68,2	P_1	0,01963	FOR , term (9)	0,12628
X	34,7	P_2	0,63764	FOR_p , term (10)	0,10448
Y	84,9	P_3	0,07253	P_2 (EST), term (11)	0,60901
$X+Y$	119,6			P_1+P_3 (EST), term (12)	0,08871
u	7			ζ , (EST), term(13)	0,78705
ω	34			FOR_p (EST), term (14)	0,10214
$u+\omega$	41			FOR_p (EST), term (15)	0,10286
NPS	3			f_3	0,00192
NUP	48			f_2	0,00840
P_s	0,05882			T_2	75,930
SP	3.278,0			T_0	84,962
SK	477,5			$f_{1,3}$	0,00135
RH	4.905,0				
λ	0,00140				
μ	0,01466				
ρ_+	0,02884				
ρ_-	0,01177				

Table 1.2 - The four-state peak load plant model parameters, the stationary probabilities of states and the other indicators of the peak load plant B

Data for the calculation of the plant parameters and the parameters of the peak load model states		Stationary state probabilities of the peak load plant		Other parameters and model indicators of the peak load plant operational conditions	
g	714,3	P_0	0,27020	P_1+P_3	0,09216
m	68,2	P_1	0,01963	FOR , term (9)	0,12628
X	34,7	P_2	0,63764	FOR_p , term (10)	0,10448
Y	84,9	P_3	0,07253	P_2 (EST), term (11)	0,60901
$X+Y$	119,6			P_1+P_3 (EST), term (12)	0,08871
u	7			ζ , (EST), term(13)	0,78705
ω	34			FOR_p (EST), term (14)	0,10214
$u+\omega$	41			FOR_p (EST), term (15)	0,10286
NPS	3			f_3	0,00192
NUP	48			f_2	0,00840
P_s	0,05882			T_2	75,930
SP	3.278,0			T_0	84,962
SK	477,5			$f_{1,3}$	0,00135
RH	4.905,0				
λ	0,00140				
μ	0,01466				
ρ_+	0,02884				
ρ_-	0,01177				

SIX-STATE (EXTENDED) MODEL OF PEAK LOAD UNIT

The six-state (extended) peak plant model is the modified four-state peak load plant model that distinguish the failure of the plant at the starting from the failure of the plant unit during the operation (Figure 2.1) [L9], [L10] and [L11]. The consequences of these failures are also different. Finally, it means that the way in which the plant failures are repaired are also different. For the four-state model data shall be collected on the durability of the repair time for all faults during the observation period that the repair frequency is calculated from the average value of these durations and the number of corresponding transitions. However, the number and type of the failures of the plant are particularly dependent on the plant operating cycle, in particular when the performance is at an early occurrence at a relatively high probability. On the other hand, for this type of failure, they are linked to relatively shorter periods of contingency, i.e. to repair, compare to the malfunctions occurring during the longer period of operation. The duty cycle inevitably has an impact on total, which means also the average repair rate of the power plant. As a result, this problem is addressed by an explicit distinction between the failures during start-up and failures during operation of the plant, and the introduction of two separate repair rates, one for the repairs following failure events at the starting and other repairs after the failures occurred during operation.



- Legend (Figure 2.1):
- “0” - the state of the plant reserve shut-down,
 - “1” - the state of the plant failure when drive is not being required, but after the failure that occurred during operation,
 - “2” - the state of the plant drive when drive is being required,
 - “3” - the state of the plant repair when drive is being required, but after the failure that occurred during operation,
 - “4” - the state of the plant when operation is not being required, but after the failure that occurred during start-up,
 - “5” - the state of the plant repair when operation is being required, but after the failure that occurred during start-up,
 - λ - the plant failure rate during operation,
 - μ_r - the plant repair rate after failure occurred during operation,
 - μ_s - the plant repair rate after failure occurred during start-up,
 - ρ_+ - the rate of occurrence of the need for the drive,
 - ρ_- - the rate of termination of the need for the drive,
 - P_s - the probability of the plant failure during the start-up.

Figure 2.1 – The six-state (extended) model of the peak load plant

According to Figure 2.1, the Markov process, which describes the six-state model of the peak load plant, describes the following system of linear differential equations:

$$\begin{aligned}
 \dot{P}_0(t) &= -\rho_+ P_0(t) + \mu_r P_1(t) + \rho_- P_2(t) + \mu_s P_4(t) \\
 \dot{P}_1(t) &= -(\mu_r + \rho_+) P_1(t) + \rho_+ P_3(t) \\
 \dot{P}_2(t) &= (1 - P_s) \rho_+ P_0(t) - (\rho_- + \lambda) P_2(t) + \mu_r P_3(t) + \mu_s P_5(t) \\
 \dot{P}_3(t) &= \rho_+ P_1(t) + \lambda P_2(t) - (\rho_- + \mu_r) P_3(t) \\
 \dot{P}_4(t) &= -(\mu_s + \rho_+) P_4(t) + \rho_+ P_5(t) \\
 \dot{P}_5(t) &= P_s \rho_+ P_0(t) + \rho_+ P_4(t) - (\rho_- + \mu_s) P_5(t)
 \end{aligned} \tag{29}$$

The initial conditions are:

$$P_0(0) = 1, P_1(0) = 0, P_2(0) = 0, P_3(0) = 0, P_4(0) = 0, P_5(0) = 0. \tag{30}$$

A stationary solution is being sought, i.e. the solution when it is

$$\dot{P}_n(t) = 0; n = 0, 1, 2, 3, 4, 5. \tag{31}$$

Under conditions (31), the system (29) takes a new form

$$\begin{aligned}
 0 &= -\rho_+ P_0(t) + \mu_r P_1(t) + \rho_- P_2(t) + \mu_s P_4(t) \\
 0 &= -(\mu_r + \rho_+) P_1(t) + \rho_+ P_3(t) \\
 0 &= (1 - P_s) \rho_+ P_0(t) - (\rho_- + \lambda) P_2(t) + \mu_r P_3(t) + \mu_s P_5(t) \\
 0 &= \rho_+ P_1(t) + \lambda P_2(t) - (\rho_- + \mu_r) P_3(t) \\
 0 &= -(\mu_s + \rho_+) P_4(t) + \rho_+ P_5(t) \\
 0 &= P_s \rho_+ P_0(t) + \rho_+ P_4(t) - (\rho_- + \mu_s) P_5(t)
 \end{aligned} \tag{32}$$

The equation of identity is:

$$P_0 + P_1 + P_2 + P_3 + P_4 + P_5 = 1 \tag{33}$$

The stationary solution, i.e. stationary state probabilities are:

$$\begin{aligned}
 P_0 &= \frac{\mu_r \mu_s (\mu_s + \rho_+) (\mu_r + \rho_+ + \rho_- + \lambda)}{\rho_+ \Delta} \\
 P_1 &= \frac{\lambda \mu_s (\mu_s + \rho_+)}{\Delta} \\
 P_2 &= \frac{\mu_r \mu_s (\mu_r + \rho_+ + \rho_-) (\mu_s + \rho_+)}{\rho_- \Delta} \\
 P_3 &= \frac{\lambda \mu_s (\mu_r + \rho_+) (\mu_s + \rho_+)}{\rho_- \Delta} \\
 P_4 &= \frac{P_s \rho_+ \mu_r (\mu_r + \rho_+ + \rho_- + \lambda)}{\Delta} \\
 P_5 &= \frac{P_s \mu_r (\mu_s + \rho_+) (\mu_r + \rho_+ + \rho_- + \lambda)}{\Delta} \\
 \Delta &= \frac{\mu_r}{\rho_+} (\mu_r + \rho_+ + \rho_- + \lambda) [\mu_s (\mu_s + \rho_+ + \rho_-) + P_s \rho_+ (\mu_s + \rho_+ + \rho_-)] + \\
 &+ \frac{\mu_s}{\rho_-} (\mu_r + \rho_+ + \rho_-) (\mu_s + \rho_+) (\lambda + \mu_r)
 \end{aligned} \tag{34}$$

The probability of the plant failure according to the six-state model is determined by the sum of the probabilities finding in the failure states, that is, states «1», «3», «4», and «5», hence:

$$P_{kvar} = P_1 + P_3 + P_4 + P_5 \tag{35}$$

In stationary conditions, the frequency of occurrence of the failure condition shall be:

$$f_{kvar} = P_1 \mu_r + P_3 \mu_r + P_4 \mu_s + P_5 \mu_s \tag{36}$$

The mean plant repair rate shall be determined by the ratio of the failure frequency and failure probability:

$$\mu_{sred} = \frac{\mu_r (P_1 + P_3) + \mu_s (P_4 + P_5)}{P_1 + P_3 + P_4 + P_5} \tag{37}$$

However, the mean plant repair rate expressed in such way is insensitive to the differences between fault types, i.e. the differences between the faults occurring at the starting and the fault conditions during the operation are not recognised, nor the differences between the conditions of repair of the plant after different failures. The mean plant repair rate by default (37) shall be equal to the plant repair rate of the four-state peak load plant model, which in accordance with the above 'hides' the different transitions from the states "1" and "4" to the state "0" or from the states "3" and "5" through the state "2" to the state "0".

For the sake of simplicity, it is possible to use the main peak load plant model with the four states as the six-state model, but subject to separate operating statistics on the rates of the transition for every single state when the plant is ready for operation, i.e. the states "0" or '2', depending on the operating cycle conditions, in particular whether the failure occurred at the starting or during the operation.

Model parameters shall be calculated in a similar manner from the operation statistics as in the baseline of the four state model, but separate statistics of the number and duration of the failures shall be introduced after the start-up and operational failures, of course, depending on whether the repairs are performed during or after the end of the operation.

The extended peak load plant model, with an adequate change, as stated for the main model of the peak load plant, can be used as a model for inclusion in the calculation of the reliability and availability indicators of the wind farm production unit.

It is necessary that special attention be given to the failures during the start of the peak load plant, which means introduction of the distinctive parameters for the probability of failure of the peak production unit at the start and the appropriate rate of repair of the plant after the start-up failures. In fact, the repair rate of the plant from the main model of the peak load plant μ in the expanded peak load plant model is "divided" into two parameters: μ_r – the peak plant repair rate after failure occurred during operation, and μ_s – the peak load plant repair rate after failure occurred during start-up. It is necessary to take account of the conditionality and the compatibility of these three parameters.

Tables 2.1 and 2.2 present the input parameters for application of the extended, the peak load stationary state probabilities so specified input parameters, and other parameters and model indicators of the peak load plant operational conditions for the peak load plants A and B, whose structures, characteristics and input data for the calculation of the model parameters are identical to those given in Tables 1.1 and 1.2. The changes in relation to the model parameters listed in Tables 1.1 and 1.2 constitute the differences between the average duration of the repairs, that is, the average duration of failures on the occurrence of the failures at the starting and the occurrence of the failures during the operation, at the end the resulting differentiation of the corresponding repair rates of the peak load plant. The model parameters for application of the six-state peak load plant model and the peak plant stationary probability of the states for the peak load plant A as results listed in Table 2.1 were obtained on the assumption that the mean peak load plant A repair rate after all failures in the phrase (37) is 0,07937. Thus, the mean value of the repair rate of the peak load plant A is equal to the repair rate of the same plant from the basic model as indicated in Table 1.1. Adequately, the model parameters for application of the six-state peak load plant model and the peak plant stationary probability of the states for the peak load plant B as results listed in Table 2.1 were obtained on the assumption that the mean peak load plant B repair rate after all failures in the phrase (37) is 0,01466. Thus, the mean value of the repair rate of the peak load plant B is equal to the repair rate of the same plant from the basic model as indicated in Table 1.2.

Table 2.1 - The six-state peak load plant model parameters, the stationary probabilities of states and the other indicators of the peak load plant A

Data for the calculation of the plant parameters and the parameters of the peak load model states		Stationary state probabilities of the peak load plant		Other parameters and model indicators of the peak load plant operational conditions	
l	0,00329	P_0	0,39638	P_{kvar} term (35)	0,05029
μ_r	0,03981	P_1	0,01637	f_{kvar} term (36)	0,00399
μ_s	0,47619	P_2	0,55333	μ_{srest} term (37)	0,07937
ρ_+	0,14706	P_3	0,02936		
ρ_-	0,10417	P_4	0,00065		
P_s	0,03191	P_5	0,00391		

Table 2.2 - The six-state peak load plant model parameters, the stationary probabilities of states and the other indicators of the peak load plant B

Data for the calculation of the plant parameters and the parameters of the peak load model states		Stationary state probabilities of the peak load plant		Other parameters and model indicators of the peak load plant operational conditions	
l	0,00140	P_0	0,26644	P_{kvar} term (35)	0,09785
μ_r	0,01130	P_1	0,01787	f_{kvar} term (36)	0,00143
μ_s	0,02857	P_2	0,63571	μ_{srest} term (37)	0,01466
ρ_+	0,02884	P_3	0,06092		
ρ_-	0,01177	P_4	0,00324		
P_s	0,05882	P_5	0,01582		

The application of the six-state peak load plant or the extended peak load plant model and the calculation of the stationary state probabilities of the peak load plant under this model are, in particular, sensitive to the ratio of the respective parameters with which the peak unit design incorporates features of the peak plant in relation to the failures at the starting and the failure conditions during the operation. In the case of peak load plant A, whose work cycles are short, often entering and leaving the drive, that is to say covering the highest parts of the power system's load diagram, the application of the extended peak load model is justified for the average time of repair of the plant after the failure during the starting which often do not last more than a few hours. In the case of the peak load plant B, whose work cycles last longer, that is to say covering the intermediate parts of the power system's load diagram, the application of the extended peak load model is justified for the average time of repair of the peak load plant after the failure during the starting which can last as long as tens of hours. Of course, in both cases, it is appropriate to take into account and correct the ratios of the peak load plants duration of repair after the failures during the operation and the failures at the starting. Any previous base on the assumption that the average repair time of the peak load plant after failure occurred during operation is significantly longer than its average repair time after failure at the starting.

Figures 2.2 and 2.3 show the results of the analysis of the corresponding repair times and the plant repair rates after the failures occurred at the starting and during operation, the average duration of the repairs and the mean repair rates on the occurrence of the all plant failures for the peak load plant A and the peak load plant B respectively.

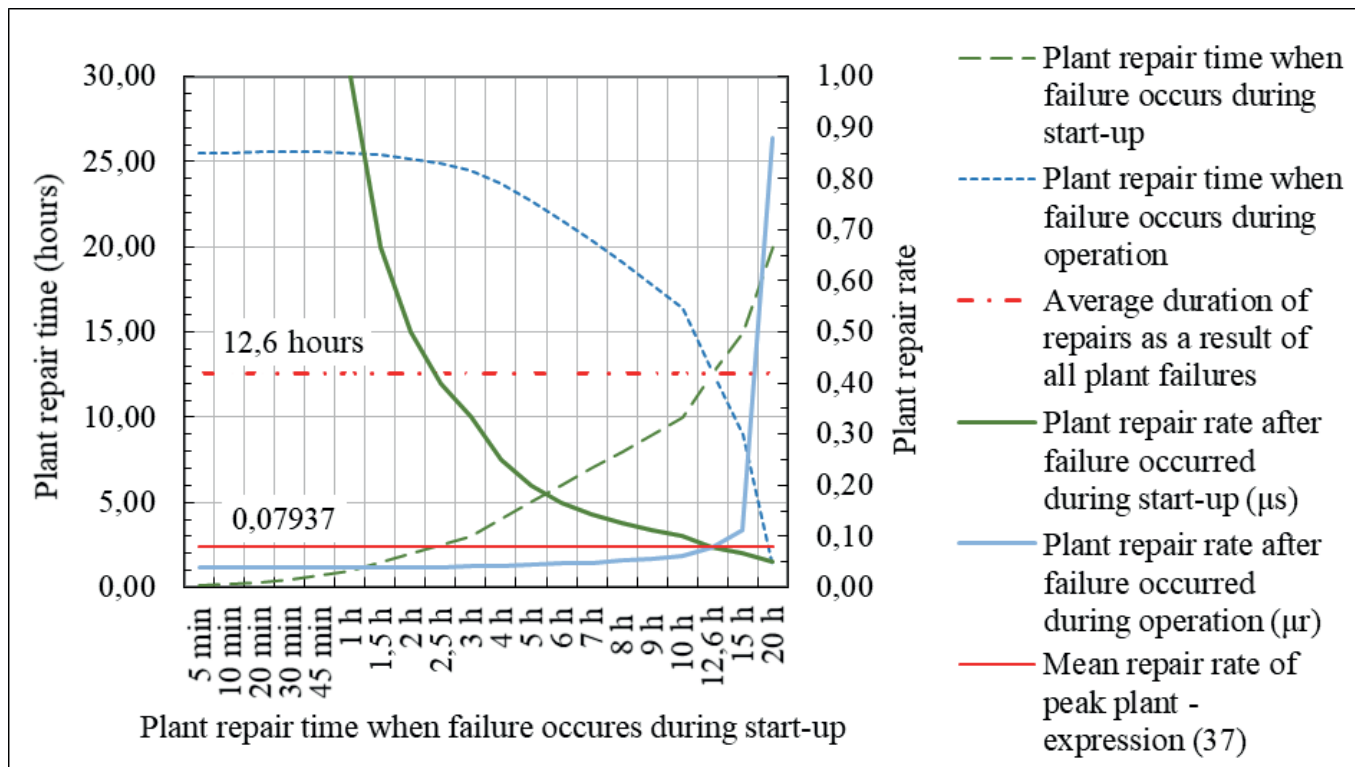


Figure 2.2 - Relationship between the repair time and repair rate, the average duration of repairs and mean repair rate for unit failures occurred during start-ups and operation – peak load plant A

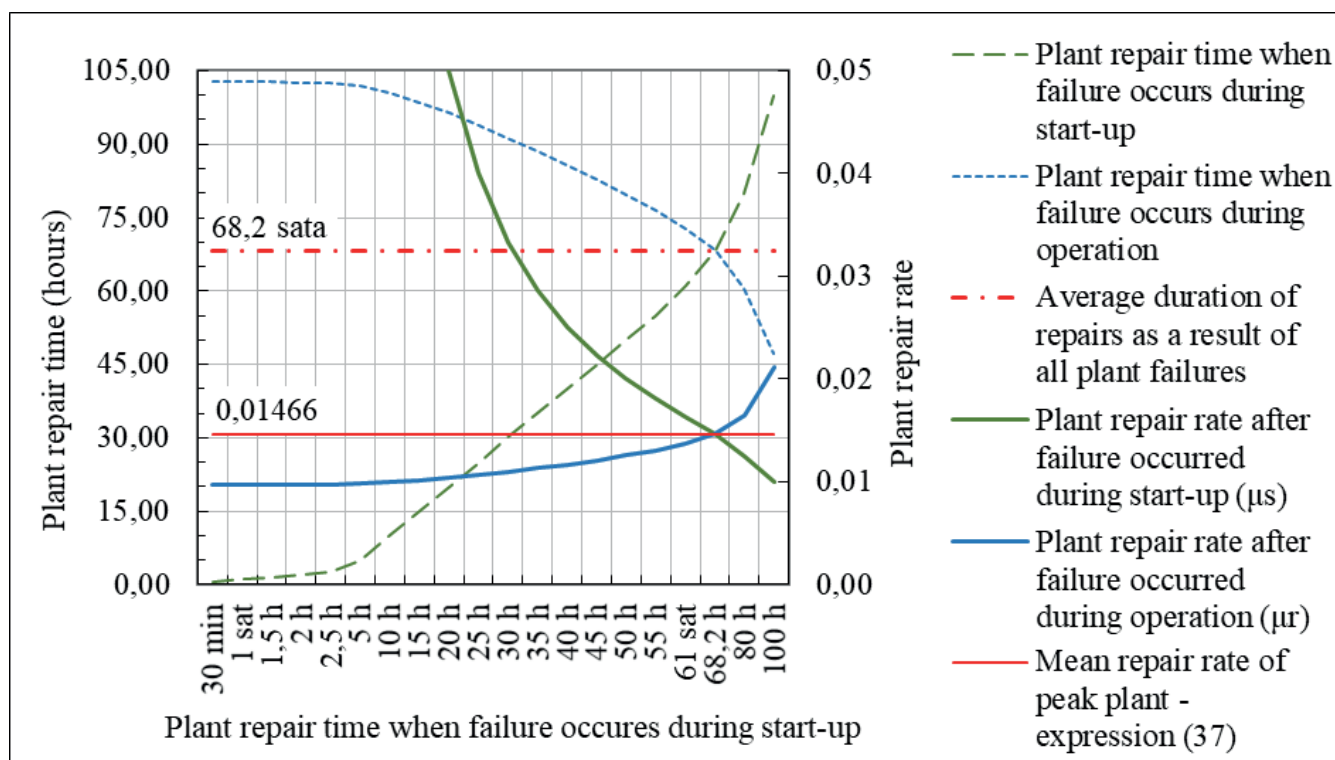


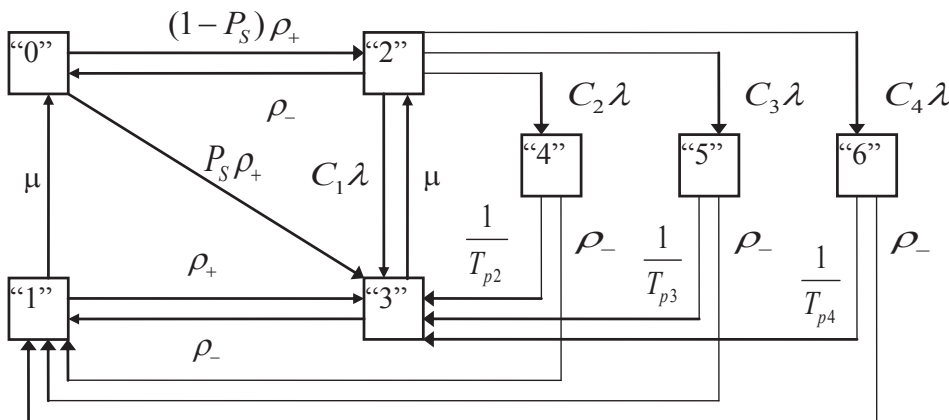
Figure 2.3 - Relationship between the repair time and repair rate, the average duration of repairs and mean repair rate for unit failures occurred during start-ups and operation – peak load plant B

SEVEN-STATE PEAK LOAD PLANT MODEL – MODEL OF PEAK LOAD PLANT WITH POSTPONABLE OUTAGES

The basis of the seven-state peak load plant model is once again the four state peak load plant model which includes some plant states that reflect the possibilities that some plant component failures would not cause outages of the plant during its operation, that is, in spite of the component failures the plant remains in operation or it is possible to postpone or delay its disconnection from the power system. When the plant will be shut down for the repair, depends of the degree of postponability. The seven-state peak load plant model as an extension includes the various postponable plant outage categories (Figure 3.1). It is obvious that greater number of the peak load plant states could be added in the basic model, each representing the separated plant postponable outage category [L9], [L10] and [L11]. At the end it is likely that some component failures could cause the plant failures that are postponable for a relatively long period of time, beyond the weekend or even longer, enabling the plant to be repaired during the period when the plant operation would not be required. This is a reason why treatment of the data and the model calibration in this case should be very precise.

The peak unit model with the possible postponement or delay in the outage or exit shall reflect the conditions when, in some cases, after the failure the plant for some period of time remains in operation because of the system needs or the other reasons. That time may be relatively long, giving the opportunity to preserve the integrity of the system by including the spare capacities or otherwise maintain the integrity of the system. On the other hand, that time must not be too long to avoid even much seriously failures. In some cases, especially in the case of the outages of the plant that have been delayed over the weekend, the failure of the plant do not in fact appear at all. It is very likely that the planned exit from the drive which has delayed for a relatively long period of time can be removed during the period in which the operation of the plant is not required. The severity of the failure is the primary criterion of the drive or removal of the plant from the operation after the failure, which may essentially be classified in four categories, namely [L9]:

- (a) immediate exit of the plant from the operation,
- (b) exit of the plant from the operation postponed for the period of up to six hours,
- (c) exit of the plant from the operation postponed from the six-hour period to the weekend, and



Legend (Figure 3.1):

- “0” - the state of the plant reserve shutdown,
- “1” - the state of the plant failure when drive is not being required,
- “2” - the state of the plant drive when drive is being required,
- “3” - the urgent unpostponable shutdown (outage) of the plant after the failure of class $i=1$,
- “4” - the postponable plant shutdown (e.g. until six o'clock) after the failure of class $i=2$,
- “5” - the postponable plant shutdown (e.g. until the weekend) after the failure of class $i=3$,
- “6” - the postponable plant shutdown (e.g. until the several days) after the plant failure of class $i=4$,
- λ - the mean rate of the all unplanned plant failures,
- μ - the plant repair rate,
- ρ_+ - the rate of occurrence of the need for the drive,
- ρ_- - the rate of termination of the need for the drive,
- P_s - the probability of the plant failure during the start-up,
- $C_i, i=1,2,3,4$ - the probability of the plant failure of class "i" during the drive,
- $T_{pi}, i=1,2,3,4$ - the mean time of the postponability after the failure of class "i".

Figure 3.1 - The seven-state peak load plant model - model with the postponable outage

(d) exits of the plant from operation postponed over the weekend.

Of course, for the peak load plants whose work cycles are short, thus covering the highest parts of the power system load diagram, the possibility to delay exit is much shorter, i.e. the maximum delay time is no longer than the few hours. Of course, in such conditions the calculation of the peak load plant model parameters is much more demanding.

As regards postponability the four-state peak load plant model, the plant failure rate λ in the general aspect shall include the possibility to delay the outage, and thus the occurrence of the unplanned outages and any part failures of the respective class, i.e. the probability that the malfunction will occur during the operation shall be of the class 1, 2 or 3. In fact, it is more accurate to say that the failure rate in the four states model represents the medium frequency of the failure which cannot be postponed over the weekend or at the time when the peak plant is not required to operate.

The influence of the explicit modelling capability of the exit from the operation is of the utmost importance for plants operating close to the base part of the power system load curve. In the case of plants with the very short operating cycles, the postponement of exit is of less importance, as that plants terminate their operation before the end of the shortest postponable time period. In many cases the effect of the postponement to the weekend will be lost. This is way the risk of the plant failure in some cases shall be reduced.

According to Figure 3.1, the Markov process, which describes the seven-state peak load plant model - the peak load plant model with postponable outages, describes the following system of linear differential equations λ :

$$\begin{aligned}
 P_0(t) &= -\rho_+ P_0(t) + \mu P_1(t) + \rho_+ P_2(t) \\
 P_1(t) &= -(\mu + \rho_+) P_1(t) + \rho_+ P_3(t) + \rho_+ P_4(t) + \rho_+ P_5(t) + \rho_+ P_6(t) \\
 P_2(t) &= (1 - P_+) \rho_+ P_0(t) - (\rho_+ + \lambda \sum_{i=1}^4 C_i) P_2(t) + \mu P_3(t) \\
 P_3(t) &= P_+ \rho_+ P_0(t) + \rho_+ P_1(t) + C_i \lambda P_2(t) - (\mu + \rho_+) P_3(t) + \frac{P_4(t)}{T_{P_2}} + \frac{P_5(t)}{T_{P_3}} + \frac{P_6(t)}{T_{P_4}} \\
 P_4(t) &= C_2 \lambda P_2(t) - (\rho_+ + \frac{1}{T_{P_2}}) P_4(t) \\
 P_5(t) &= C_3 \lambda P_2(t) - (\rho_+ + \frac{1}{T_{P_3}}) P_5(t) \\
 P_6(t) &= C_4 \lambda P_2(t) - (\rho_+ + \frac{1}{T_{P_4}}) P_6(t)
 \end{aligned} \tag{38}$$

The initial conditions are:

$$P_0(0) = 1, P_1(0) = 0, P_2(0) = 0, P_3(0) = 0, P_4(0) = 0, P_5(0) = 0, P_6(0) = 0. \tag{39}$$

A stationary solution is being sought, i.e. the solution when it is

$$\dot{P}_n(t) = 0, n = 0, 1, 2, 3, 4, 5, 6. \tag{40}$$

Under conditions (40), the system (38) takes the form of:

$$\begin{aligned}
 0 &= \rho_+ P_0(t) + \mu P_1(t) + \rho_+ P_2(t) \\
 0 &= (\mu + \rho_+) P_1(t) + \rho_+ P_3(t) + \rho_+ P_4(t) + \rho_+ P_5(t) + \rho_+ P_6(t) \\
 0 &= (1 - P_+) \rho_+ P_0(t) - (\rho_+ + \lambda \sum_{i=1}^4 C_i) P_2(t) + \mu P_3(t) \\
 0 &= P_+ \rho_+ P_0(t) + \rho_+ P_1(t) + C_i \lambda P_2(t) - (\mu + \rho_+) P_3(t) + \frac{P_4(t)}{T_{P_2}} + \frac{P_5(t)}{T_{P_3}} + \frac{P_6(t)}{T_{P_4}} \\
 0 &= C_2 \lambda P_2(t) - (\rho_+ + \frac{1}{T_{P_2}}) P_4(t) \\
 0 &= C_3 \lambda P_2(t) - (\rho_+ + \frac{1}{T_{P_3}}) P_5(t) \\
 0 &= C_4 \lambda P_2(t) - (\rho_+ + \frac{1}{T_{P_4}}) P_6(t)
 \end{aligned} \tag{41}$$

The equation of identity is:

$$P_0 + P_1 + P_2 + P_3 + P_4 + P_5 + P_6 = 1 \tag{42}$$

The stationary solution, i.e. the stationary state probabilities are:

$$\begin{aligned}
 P_0 &= \frac{\mu [\mu + \rho_+ + \rho_+ + \lambda(\mu A + C)]}{\rho_+ \Delta} \\
 P_1 &= \frac{\lambda(\mu A + C) + P_+ \rho_+}{\Delta} \\
 P_2 &= \frac{\mu \left[\frac{1}{\rho_+} (\mu + \rho_+) + 1 - P_+ \right]}{\Delta} \\
 P_3 &= \frac{\frac{1}{\rho_+} [(\mu + \rho_+) (\lambda C + P_+ \rho_+)] - (1 - P_+) \lambda \mu A}{\Delta} \\
 P_4 &= \frac{T_{P_2} C_2}{\rho_+ T_{P_2} + 1} \frac{\lambda \mu \left[\frac{1}{\rho_+} (\mu + \rho_+) + 1 - P_+ \right]}{\Delta} = A_1 \lambda P_2 \\
 P_5 &= \frac{T_{P_3} C_3}{\rho_+ T_{P_3} + 1} \frac{\lambda \mu \left[\frac{1}{\rho_+} (\mu + \rho_+) + 1 - P_+ \right]}{\Delta} = A_2 \lambda P_2 \\
 P_6 &= \frac{T_{P_4} C_4}{\rho_+ T_{P_4} + 1} \frac{\lambda \mu \left[\frac{1}{\rho_+} (\mu + \rho_+) + 1 - P_+ \right]}{\Delta} = A_3 \lambda P_2
 \end{aligned} \tag{43}$$

where:

$$\begin{aligned}
 \Delta &= \frac{\mu}{\rho_+} [\mu + \rho_+ + \rho_+ + \lambda(\mu A + C)] + \mu \left[\frac{1}{\rho_+} (\mu + \rho_+) + 1 - P_+ \right] + \\
 & \quad [\lambda(\mu A + C) + P_+ \rho_+] \left[1 + \frac{1}{\rho_+} (\mu + \rho_+) \right] \\
 A_1 &= \frac{T_{P_2} C_2}{\rho_+ T_{P_2} + 1} \quad A_2 = \frac{T_{P_3} C_3}{\rho_+ T_{P_3} + 1} \quad A_3 = \frac{T_{P_4} C_4}{\rho_+ T_{P_4} + 1} \\
 A &= A_1 + A_2 + A_3 \\
 C &= C_1 + C_2 + C_3 + C_4 = 1
 \end{aligned} \tag{44}$$

In contrast to the terms for the stationary state probabilities of the main four-state peak load plant model, i.e. P_0, P_1, P_2 and P_3 , in the corresponding terms using the seven-state model, i.e., P_0, P_1, P_2 and P_3^* , the plant failure rate λ is further multiplied by the term $(\mu A + C)$, i.e. $(\mu A + 1)$. The failure rate of the plant in the four-state plant model may be taken with an equivalent size of multiplying the value of the seven-state model, and vice versa.

On the other hand, term P_3 is the sum of the probabilities of different degree of the plant failures, i.e. the sum of the postponable outage states »3«, »4«, »5«, and »6«, hence

$$P_3^* = P_3 + P_4 + P_5 + P_6 = \frac{1}{\rho_+} \left\{ (\mu + \rho_+) [\lambda(\mu A + C) + P_+ \rho_+] \right\} \tag{45}$$

where:

Δ - as in the phrase (44).

then the term for the probability of the state »3«, i.e. the state the immediate exit after the failure class $i=1$ may be written in the following format:

$$\begin{aligned}
 P_3 &= P_3^* - (P_4 + P_5 + P_6) = P_3^* - \lambda A P_2 = \\
 &= \frac{1}{\rho_+} \left\{ (\mu + \rho_+) [\lambda(\mu A + C) + P_+ \rho_+] \right\} - \frac{\lambda A \mu [(\mu + \rho_+) + (1 - P_+) \rho_+]}{\Delta}
 \end{aligned} \tag{46}$$

where:

Δ - as in the phrase (44).

The probability of the plant failure in the four-state model can be considered equivalent to the sum of the different degrees of the outage delay in the modelling of the contingencies with the seven-state model. This means that the additional operation conditions of the peak plant which is explicitly delayed by the outages can be seen as an »expansion« of the states »3« in four-state model. When certain parameters T_{P_i} ; $i=2,3,4$ and ρ_+ , i.e. the mean time for postponable outage of the plant after the failure of class "i" and the rate of termination of the need for the drive, are known, it can easily be observed that the relationship of the probability ratio of the state »3« (the state for which the failure causes the emergency outage of the plant) and the states »4«, »5«, and »6« determines only the probability of the failure of the defined class of the failure »i«, i.e. C_i ; $i=1,2,3,4$.

The operation statistics shall correspond, in essence, to the operational statistics of the main four-state peak load plant model, with the addition of the above parameters, which is in effect the state »3« in the base model, on a number of situations characterised by the probability of occurrence and times of duration.

Tables 3.1 and 3.2 present for the peak load plant A and the peak load plant B the input data for calculating the parameters of the peak plant model operational states and the possible postponement of exit from the drive, the stationary probability of these peak load plant states for the input parameters so defined and the other parameters of the seven-state peak model of the peak load plants A and B. The change in relation to the model parameters listed in Tables 1.1 and 1.2 constitutes a distinction between different categories of the delay of exit of the completed plant.

Also with regard to the application of the peak load plant model with the possible delay in the contingency or exit from the operation the model input parameters and the stationary probabilities of the peak plant states are determined by the location and operating mode of the generation plant in the power system. However, as this is not a significant conditionality, the choice of the averaging periods after different failure classes during operation of the peak plant is not limited in advance. However, it is appropriate to adapt it to the operational requirements placed on a specific peak power plant, in particular to bring it into line with the corresponding operating cycles of the peak power plant.

Table 3.1 – The seven-state peak load plant model parameters, the stationary probabilities of states and the other indicators of the peak load plant A

Data for the calculation of the plant parameters and the parameters of the peak load model states		Stationary state probabilities of the peak load plant		Other parameters and model indicators of the peak load plant operational conditions	
λ	0,00329	P_0	0,39916	P_3^* , term (45)	0,03366
μ	0,07937	P_1	0,01547	P_3 , term (46)	0,03103
ρ_+	0,14706	P_2	0,55171		
ρ_-	0,10417	P_3	0,03100		
P_s	0,03191	P_4	0,00023		
C_1	0,34000	P_5	0,00098		
C_2	0,27000	P_6	0,00145		
C_3	0,21000				
C_4	0,18000				
T_{p2}	0,50				
T_{p3}	3,50				
T_{p4}	8,00				

Table 3.2 – The six-state peak load plant model parameters, the stationary probabilities of states and the other indicators of the peak load plant B

Data for the calculation of the plant parameters and the parameters of the peak load model states		Stationary state probabilities of the peak load plant		Other parameters and model indicators of the peak load plant operational conditions	
λ	0,00140	P_0	0,26864	P_3^* , term (45)	0,07831
μ	0,01466	P_1	0,02116	P_3 , term (46)	0,07037
ρ_+	0,02884	P_2	0,63189		
ρ_-	0,01177	P_3	0,07027		
P_s	0,05882	P_4	0,00113		
C_1	0,34000	P_5	0,00263		
C_2	0,27000	P_6	0,00429		
C_3	0,21000				
C_4	0,18000				
T_{p2}	5,00				
T_{p3}	17,00				
T_{p4}	38,00				

Finally, Figures 3.2 and 3.3 show the stationary state probabilities of the peak load plant A and the peak load plant B respectively, calculated according to the basic four state peak load model, the six-state peak load model (extended) and the seven-state peak load model with the possible delay in exiting the plant from drive.

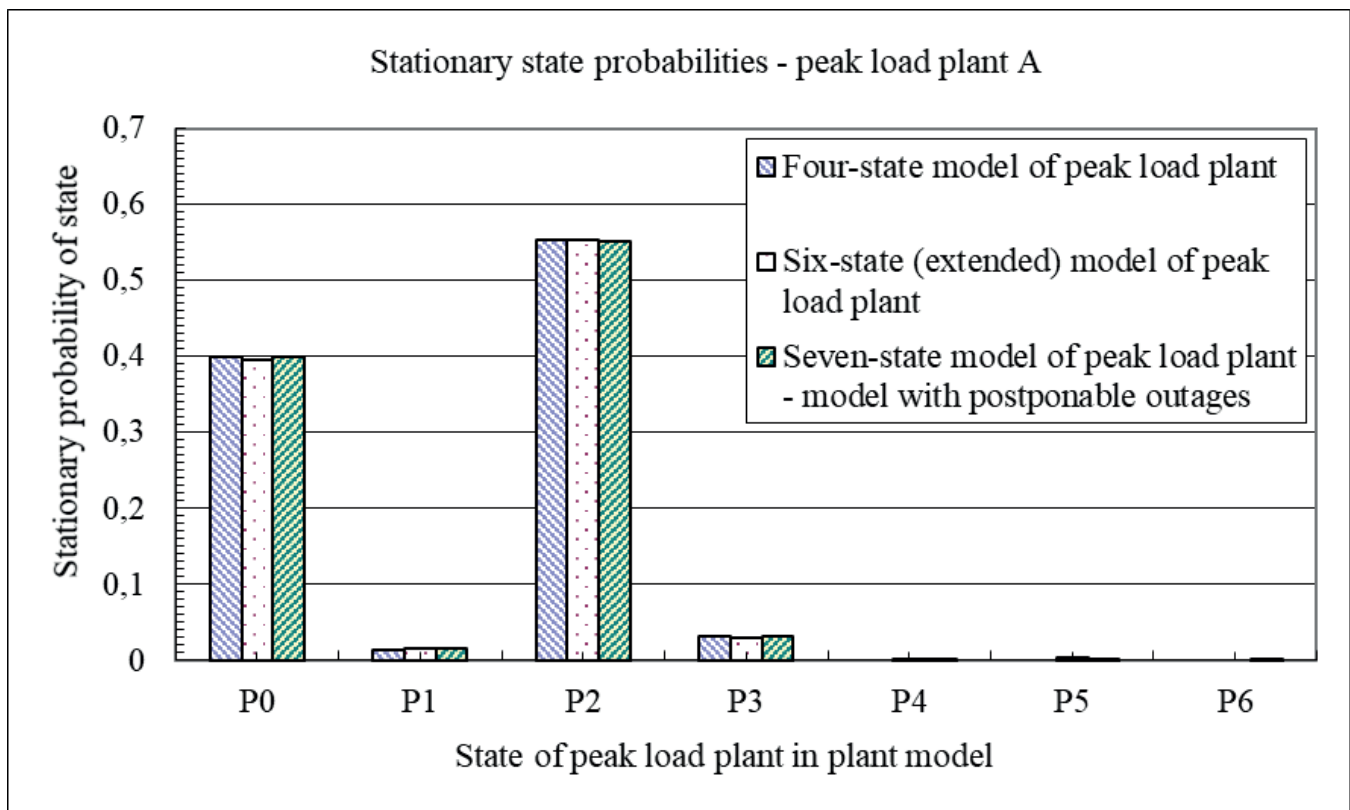


Figure 3.2 – The stationary state probabilities of the peak load plant A in the peak plant models

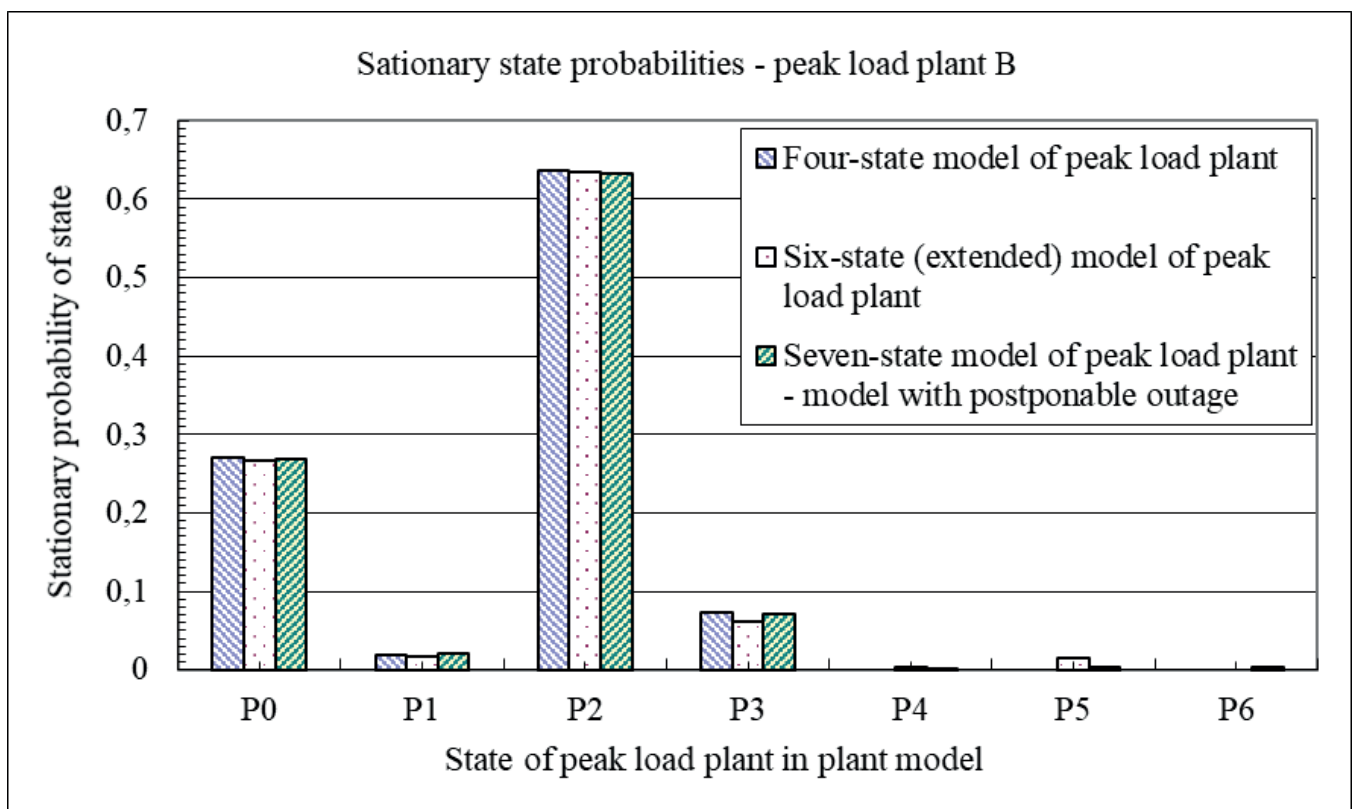


Figure 3.3 – The stationary state probabilities of the peak load plant B in the peak plant models

CONCLUSION

The peak load plant models have been developed and exposed to calculate the reliability and availability parameters and indicators that the peak generating plants include in the reliability and availability patterns of the power systems when operating schedules. The developed models, hence the associated reliability and availability indicators are dictated by the technical and energy characteristics of the plants that cover the peak load curve, i.e. the peak part of the power system load profile, but they also include and reflect the specific conditions and requirements that can be installed in the facilities or from the operation on such facilities in view of the dynamics resulting from their location and role in covering the load and the consumption of the power system. In particular, through the separate

different models for the calculation of the parameters and indicators of reliability and availability of peak load plants, they include the possibility of explicit differentiating between the failures at the start and during the operation, which are usually different in terms of the severity of the effects, including the duration of the repairs, and the possibility to delay the outage or removal from the drive through several categories of the peak plant outage deferral.

Each of the expose peak load plant model was applied on the peak load plants with the different operating cycle durations and operating requirements, the model parameters and other modelling parameters and indicators have been calculated, demonstrating the applicability of the peak load plant models.

REFERENCES

- [1] MIKULIČIĆ, V., Matematički modeli pouzdanosti i raspoloživosti u elektroenergetskom sustavu, Doktorska disertacija, Sveučilište u Zagrebu, Elektrotehnički fakultet, Zagreb, 1981.
- [2] MIKULIČIĆ, V., Matematički model pouzdanosti komponente, Elektrotehnika EKTTBV24(1981)1, 1981.
- [3] JÖZSA, L., Primjena metode pouzdanosti u izgradnji proizvodnih kapaciteta u sustavu hidro i termoelektrana, Elektrotehnika EKTTBV24, 1981.
- [4] Studie Systemzuverlässigkeit, Institut für Elektrische Anlagen und Energiewirtschaft, R.W.T.H. ACHEN, 1982
- [5] BILLINTON, R., ALLAN, R. N., Reliability Evaluation of Power Systems, New York, 1984
- [6] JÖZSA, L., Analički model pouzdanosti akumulacijskih hidroelektrana, I i II dio, Elektrotehnika ELTHB2 28, 1985.
- [7] BILLINTON, R., ALLAN, R. N., Reliability Assessment of Large Electric Power Systems, Kluwer Academic Publishers, Boston, 1988
- [8] INVERNIZZI, A., MANZONI, G., RIVOIRO, A., Probabilistic Simulation of Generating System Operation Including Seasonal Hydro Reservoirs and Pumped-Storage Plants, Electric Power & Energy Systems, Vol. 10, No. 1, 1988
- [9] SOETHE J.R., PATTON, A. D., A Comparison of Alternative Generating Unit Reliability Models, IEEE Transactions on Power Systems, Vol. 4, No. 1, February 1989, 108-114.
- [10] BILLINTON, R., LI, W., Reliability Assessment of Electric Power Systems Using Monte Carlo Methods, New York, 1994
- [11] KLEPO, M., Pouzdanost i raspoloživost elektroenergetskog sustava pri operativnim planiranjima rada, Doktorska disertacija, Sveučilište u Zagrebu, Fakultet elektrotehnike i računarstva, Zagreb, 1996.
- [12] KLEPO, M., Model neizvjesnosti pojave opterećenja u modelu pouzdanosti i raspoloživosti elektroenergetskog sustava, Energija, god.46(1997), br. 3.
- [13] KLEPO, M., Modeli proizvodnih jedinica u modelu pouzdanosti i raspoloživosti elektroenergetskog sustava – model bazne jedinice, Energija, god.46(1997), br. 4.
- [14] KLEPO, M., MIKULIČIĆ, V., ŠIMIĆ, Z., Model crpno-akumulacijske (reverzibilne) hidroelektrane u modelu pouzdanosti i raspoloživosti elektroenergetskog sustava, Energija, god. 57(2008), br. 1., str. 38-63
- [15] MIKULIČIĆ, V., ŠIMIĆ, Z., Modeli pouzdanosti, raspoloživosti i rizika u elektroenergetskom sustavu, I. dio, Udžbenik Sveučilišta u Zagrebu, Svibanj 2008.
- [16] M. Klepo, V. Mikuličić, Z. Šimić: Model proizvodne jedinice s uključenim uvjetima okoline u modelu pouzdanosti i raspoloživosti elektroenergetskog sustava; Energija, god. 58 (2009), br. 1.; 26-55

